ABSTRACT

An Investigation into the Electrical, Optical, and Microstructural Effects of Aluminum-Doping Amorphous Indium Zinc Oxide via Ultra-High Vacuum Co-Sputter Deposition

Austin S. Reed, M.S.M.E.

Mentor: Alexandre Yokochi, Ph.D.

Indium Zinc Oxide (IZO) has emerged as a high-potential candidate for electronic applications involving novel flexible and transparent devices. IZO's rapid growth is attributed to its high carrier mobility (~40-50 cm^2/Vs) [1-4], room-temperature fabrication [1,2,5-7], superb transparency (>85%) [2,3,8-12], and conducting/semiconducting capabilities [13,14]. While IZO's high carrier density (~10^{20} cm^{-3}) has prevented immediate application as a semiconductor [15-18], strategies to lower the carrier density into the semiconducting range have emerged (<10^{17} cm^{-3}) [1,8,18]. Recently, novel doping techniques have demonstrated success in deterring IZO's carrier generation while maintaining both its microstructural and optoelectrical properties. This study investigates the effects of doping IZO thin films with Al^{3+} via ultra-high vacuum co-sputter deposition. Films were fabricated at room-temperature (~25ºC) implementing direct-current and radio-frequency power sources for IZO and Al^{3+}, respectively. An effective carrier suppression of ~10^3 cm^{-3} at RF-25W was observed, as well as the enhancement of amorphous-phase stability via Al^{3+}-inclusion in IZO.

An Investigation into the Electrical, Optical, and Microstructural Effects of Aluminum-Doping Amorphous Indium Zinc Oxide via Ultra-High Vacuum Co-Sputter Deposition

by

Austin Reed, B.S.M.E.

A Thesis

Approved by the Department of Mechanical Engineering

_____

Paul Ro, Ph.D., Chairperson

Submitted to the Graduate Faculty of
Baylor University in Partial Fulfillment of the
Requirements for the Degree
of

Master of Science in Mechanical Engineering

Approved by the Thesis Committee

_____

Alex Yokochi, Ph.D., Chairperson

_____

Annette von Jouanne, Ph.D.

_____

Yue Ling, Ph.D.

Accepted by the Graduate School

May 2019

_____

J. Larry Lyon, Ph.D., Dean

Page bearing signatures is kept on file in the Graduate School.

TABLE OF CONTENTS

LIST OF FIGURES

LIST OF TABLES

ACKNOWLEDGMENTS

First and foremost, I cannot thank Dr. Lesley Wright enough for her unconditional support throughout my time at Baylor. Dr. Wright played a substantial role in developing me into the person I am today, and without her there is not a chance I would have made it through. During my first semester in graduate school, she was the sole reason I didn't collapse in on myself as she brute-forced me into not giving up, and for that I am perpetually grateful. While we are, and I cannot emphasize this enough, very different people, I consider her to be my perpetual mentor, an unsurpassable role-model, and a dear friend.

Additionally, I want to thank Dr. Douglas Smith for, more than anyone else, listening to me. When my anxiety and hopelessness pushed me to the breaking point, he provided a space free from judgment and motivated me to keep moving forward. Furthermore, Dr. Smith's FEA class was the first and only class that I thoroughly enjoyed throughout the entirety of my academic career and I looked forward to it every single day.

Dr. Alex Yokochi deserves all the gratitude in the world, as he not only accepted me into his group with open arms but singlehandedly pushed me to stand in front of my peers and defend my thesis. Dr. Yokochi never gave up on me despite my best attempts to make him do so, even after months of me providing no communication and dropping off of the grid. At a moment where angst truly crippled me, Dr. Yokochi literally sat me down and drove me to finish, refusing to let me fail. Furthermore, Dr. Yokochi, alone, re-kindled

the passion and curiosity I once had for research and I cannot thank him enough for all that he's done for me. There is no better place I could have landed than under his guidance.

Regarding Barah Ahn and Grant Dreweloe, no words can express how truly grateful I am that these two wonderful people entered my life. They provided me with unparalleled friendships and the experiences we endured together brought us closer than I could have ever imagined. Chandon Stone and Ugo Ugwu showed me how amazing it is to watch a group of people grow as both researchers and individuals. The experiences I had both working with and mentoring them is something I'll cherish for the rest of my life.

Michael and Sam, you gave me a home in Waco when I moved away. I'm proud to call you my friends and I am fortunate to know people like you. I can never accurately state how valuable I consider our friendships and how overjoyed I am about the fact that you consider me an uncle of Emersyn's.

I would also like to say thank you to Dr. Stanley Ling and Dr. Annette von Jouanne as they, with no background on my work nor any notion of who I was, provided unwavering support throughout my mentally-taxing defense and my only regret is that I would have met them sooner.

I would also like to thank Dr. Steve Dworkins and Dr. Carlos Manzanares for letting our group using their equipment in the BSB as this project could not have been completed without it

To my parents, whom I owe everything

To Jackson, my dearest friend

To Brady, for an eternal competition

To Chase, you provided an escape

To Papa, the gadfly in my life

To Grandma, a light in the dark

To my pets, dogs should live longer than humans

To my mental health, you almost won

To the Republic, for democracy

CHAPTER ONE

Introduction

1.1 Amorphous Oxide Thin Films

Recently, numerous amorphous oxide materials have emerged as promising candidates for use in both semiconductor and conductor applications. Due to their low resistivities (~10^4 Ω-cm) [9,21-23] and high transparencies in the visible regime (>80%)[9,17,22,23], amorphous oxide semiconductors (AOSs) and amorphous transparent conducting oxides (TCOs) show increasing promise in realizing the development and implementation of novel flexible and transparent optoelectronic devices.

The argument for the utilization of amorphous oxides over current amorphous-Silicon (*a*-Si) technology holds substantial weight due to their ability to be fabricated at room temperature (~25ºC–200ºC) [1,7,8,18,24], tunable optoelectronic properties [1,6,9-11,15,25-30], excellent surface uniformity [3,8,15,16,31,32], and higher carrier mobilities (>10-30 cm^2/Vs) in respect to *a*-Si:H (<1 cm^2/Vs) [1,8,9,15,18,22,33]. Furthermore, because amorphous oxide thin films are developed in an amorphous phase rather than a semi-/poly-crystalline phase, the absence of grain boundary defects [1,6,32] indicates strong potential for use in multi-layered optoelectronic device applications.

Among the numerous amorphous oxide candidates suitable for device implementation, In_2O_3-based compounds have earned substantial notoriety due to their exceptional hall carrier mobilities (≥20 cm^2/Vs) [1-3,9,32,34,35]. However, while In_2O_3-based amorphous oxides possess remarkably high carrier mobilities their practicality in

applications depends significantly on the stability of the amorphous phase[23,31,35]. Though pure-In_2O_3 and commonly-used Sn-doped In_2O_3 (ITO) thin films both possess desirable optoelectronic and microstructural characteristics, the instability of their amorphous phases causes the materials to undergo microstructural crystallization around temperatures of ~125^oC [23,31,35]. To address the issue of amorphous-phase instability in In_2O_3 films, numerous studies have investigated the amorphous phase effects of introducing a ternary cation dopant to the In_2O_3-matrix as well as examining the subsequent alterations the dopant may have on the films' optoelectronic characteristics[7,13,15,31,36,37]. In particular, the doping of In_2O_3 with 10 wt. % ZnO (IZO) has shown to effectively delay the onset-of-crystallization of the amorphous state to temperatures as high as ~500^oC in ~1-2hr air anneals, substantially increasing the thermal stability of the thin films[1,9,10,28,38]. In addition to its enhanced amorphous-phase stability, IZO has exhibited outstanding application potential as it also possesses unique optoelectronic abilities suitable for high-performance devices. Key characteristics – on top of enhanced amorphous-phase stability – which justify further investigation of IZO are listed below, along with some of the distinct qualities which validate its superior-candidacy for application in comparison to other commonly used amorphous oxide materials:

(1) First-rate transparency in the visible regime (>85% transmittance) [2,3,8-12]

(2) Highest electron carrier mobility (up to ~50 cm^2/Vs) [1,2,9] among leading AOSs

(3) Ability to be fabricated at room temperature [2,5-7,39,40], allowing for electronic device production on flexible substrates such as plastics, composites, and papers

(4) Wide-range tunability of *a*-IZO's electron carrier concentration [1,14,15,40], permitting high-impact multilayered IZO devices, e.g. IZO channel/IZO metallization TFTs [14]

The unique combination of these defining characteristics distinguish IZO as one of the most promising AOS materials and exhibit high potential for application in areas such as, but not limited to, thin film solar cells, ultra-high resolution (UHR) displays, and thin film transistors (TFTs).

The wide-range tunability of IZO's electron carrier concentration, mentioned in Step (4) above, is a promising quality of IZO still under study as IZO in its as-deposited state possesses an intrinsically high carrier concentration (~10^{20} cm^{-3})[1,15,28,41], limiting its use in semiconducting applications where lower carrier concentrations (<10^{17} cm^{3}) are required. To date, several methods have proved to be effective in suppressing the carrier concentration of IZO such as the introduction of ternary cation dopants[15,18,34,37,39,40,42-47], varying O_2 concentration during fabrication of IZO[1,48], and post-fabrication film treatments (UV exposure, annealing, etc.)[25,41,49]. Effectively controlling IZO's carrier mobility introduces the promising capability of developing multi-layered electronic devices comprised of multiple IZO-based layers - which has been shown to have strongly beneficial effects in terms of lowering the interfacial contact resistance which normally forms between dissimilar materials[14]. In general, it has been shown that ternary-/quaternary-doped IZO compounds possess lower mobility (~5-15 cm^2/Vs) than binary IZO as the dopants act as scattering centers, diminishing *a*-IZO's desirable carrier transport properties[1,15,50,51]. However, the ternary-doped IZO compounds' carrier mobilities do not eliminate them as promising

candidates for application, as other unknown qualities may emerge during the fabrication and analysis processes – as seen by the rapid surge of IGZO display devices and IGZO TFT research[31,36,39,40,52]. The ternary dopant materials which can be selected for investigation are limited to an extent, as a general combination of certain element characteristics tends to make a material more suitable for selection than others, such as Lewis Acid strength, ionic radius, dopant-bonding strength to oxygen, and effective core potential[15]. Thus, if a potential dopant material comes close to what defines an ideal doping cation, it is justifiable to state that further investigation into the effects that unexplored ternary-cation dopants may have on the optoelectrical and microstructural properties of IZO.

This study, in particular, provides a look into an initial investigation of the electrical, optical, and microstructural effects of doping IZO with aluminum (Al^{3+}) through utilizing a UHV co-sputter deposition technique. As Al^{3+} has not been thoroughly investigated for its potential use as an *a*-IZO-dopant (even though Al^{3+} possesses properties which identify it as an ideal ternary-dopant cation[15]), an initial investigation of Al^{3+}-doped IZO should provide insight towards its potential use as a viable *a*-IZO-dopant. Via UHV co-sputter deposition, Al^{3+}-doped *a*-IZO films were fabricated with incrementally increasing concentrations of Al^{3+}-content in the In-Al-Zn-O (IAZO) films. As meaningful energy-dispersive X-ray spectroscopic (EDX) data could not be obtained due to the thinness of the films (~100 nm) as well as the time limitations of the study, the increasing content of Al^{3+}-dopant material in each thin film is classified by the radio-frequency (RF) power at which the Al3+-target was set at instead of the more commonly used wt. %. Thus, in respect to increasing dopant material, the RF power ranged from 0W to 25W in

increments of 5W, excluding RF powers of <10W. Reliable films could not sufficiently be fabricated at powers <10W due to the low power sputter settings resulting in a flickering/non-steady RF plasma beam. RF-25W was selected, post-fabrication, as the maximum dopant concentration investigated due to film analysis revealing films fabricated at powers >25W films became reflective, losing their transparent quality due to a surplus of Al^{3+} content in the films.

1.2 Thesis Overview

This thesis explores the implementation of a unique co-sputter deposition method to investigate the effects of Al^{3+}-doping amorphous In-Zn-O, a promising and newly emerging amorphous oxide semiconductor. In total, this thesis has five chapters detailing the iterative and experimental techniques utilized for an in-depth examination of IAZO. Chapter Two provides a comprehensive background of thin films and amorphous oxides, as well as a history of *a*-IZO through its developing into a promising metal-oxide possessing both semiconducting and conducting capabilities. Chapter Two also describes previous investigations of different *a*-IZO-doping techniques and their potential for use.

In Chapter Three, the iterative and experimental techniques implemented in this study to both fabricate and analyze IAZO thin films developed are described in full detail. First, sputter deposition parameters are defined, explaining each fabrication process and the methods used to ensure the development of quality samples. The iterative methods used to determine the proper sputter parameters for developing IAZO films are then described, specifying each step implemented, as well emphasizing how final fabrication parameters were selected. To conclude Chapter Three, the qualitative techniques used for film characterization are broken down into three categories: electrical, optical, and

microstructural. Each method's objective and justifications for use are extensively detailed along with the background theory behind the techniques.

Chapter Four provides a thorough investigation of the data and results found from the analysis of the aluminum-doped films, once again broken down into three categories: electrical, optical, and microstructural. Crossover between categories occurs in some cases, due to the related changes in the materials directly causing one property to change with another (e.g. some electric properties directly impact optical properties and vice versa). Film characteristics are expansively discussed in Chapter Four, emphasizing the impact of aluminum-doping on *a*-IZO's application potential as well as what the study's results imply moving forward.

In Chapter Five, the study's significant findings are first concluded, fully summarizing the meaningful results and conclusions gathered as well as what must be done before fully realizing IAZO's potential. Brief overviews of other thin film-oriented work done by the student over the duration of the master's program are also described, such as contributions in journal papers and other projects worked throughout the time allotted.

1.3 Research Objective

This thesis provides an initial investigation into the electrical, optical, and microstructural effects of Al^{3+}-doping *a*-IZO thin films. Through the iterative and experimental method of IZO and Al^{3+} UHV co-sputter deposition, researchers hoped to better understand the effects which Al^{3+}-doping may have on IZO's application potential and amorphous oxide performance. Numerous IAZO samples were fabricated in order to establish the validity of the results presented, as well as providing affirmation for any impactful discovery found in the resulting data. Post-fabrication analysis consists of an in-

depth optoelectronic examination of electron carrier transport properties, as well as providing an initial investigation into the microstructural effects of Al^{3+}-doping IZO thin films.

CHAPTER TWO

Literature Review

2.1 Thin Film and Amorphous Oxide Background

In the midst of the Fourth Industrial Revolution[53,54], thin film micro-/nano-optoelectronics have risen to be among the strongest drivers of both economic and technological progress[55]. Largely responsible for the exponential development and innovation of display applications, information storage and processing, clean energy technologies, and biotechnologies over recent years, thin films have attracted significant interest, particularly in the field of academic research.

In general, thin films are fabricated through the condensation (deposition) of individual atoms onto an independent material known as a substrate (glass, silicon, etc.)[56]. Typically, thin film layers are less than five microns in thickness, where a certain material's characteristics such as film uniformity, microstructural phase/orientation, conductivity, film transparency, etc. dictate potential fields of application[56]. Recently, the development of high-performance transistors based on thin film technology has been accredited as the backbone of optoelectronic progress[57], catalyzing innovation in devices such as microprocessors, solid-state memories, graphics adapters, UHR displays, solar cell technology, smart-emissivity coatings, and countless more. Out of the many thin film materials currently employed, as well as those still under investigation, amorphous oxide thin films have shown substantial promise implementation due to possessing the ability to be grown on flexible substrate while maintaining high-performance optoelectronic

properties[8,16-18,24]. Additionally, an exclusive advantage which amorphous oxides hold over their crystalline counterparts is the ability to uniformly fabricated over large-areas at low fabrication temperatures[16] - a valuable trait which has led to *a*-Si:H becoming the central pillar for the development of active-matrix flat-panel displays[16].

While amorphous oxide thin films, as a whole, possess a vast assortment of desirable thin film qualities, it is widely accepted that there is no feature more important than that of their controllable optoelectrical properties[8,16-18,24]. The resistivity of a thin film, ρ, sometimes expressed by its inverse, conductivity, σ, determines a material's ability to resist the flow of electric current[58]. The ability to tune the resistivity of an amorphous oxide provides an invaluable method of optimizing a desired material's optoelectrical properties to fit a specific application. If the thin film material is an n-type semiconductor (i.e. majority carriers are electrons, p-type semiconductor = holes) similar to the films investigated in this paper, the resistivity is directly dependent on two material characteristics: (i) carrier mobility and (ii) carrier concentration. The electron mobility of a film, μ, is defined as the velocity at which free electrons may drift throughout the material when subjected to an electric field[58] whereas the carrier density (concentration) of a film, n, is the density of free electrons within the material[58]. High mobility amorphous oxides are of particularly high interest among thin film applications as it has been shown that, through various during-/post-fabrication techniques, amorphous oxide carrier densities can be repeatably and reliably tuned to fit a desired application[1,15,18,25,34,37,39-49] . Consequently, as mentioned in Section 1.1, a recent emergence of In_2O_3-based amorphous oxides has taken place due to their characteristically high carrier mobilities[1-3,9,32,34,35] in comparison to other amorphous oxide materials.

2.2 The Emergence of Indium Zinc Oxide

Out of the many In_2O_3-based amorphous oxide conductors, Sn-doped In_2O_3 (ITO) has dominated commercial application due to an established knowledge about both its capabilities and limitations brought upon through decades of extensive research[23,35,59-64]. However, ITO is drastically restricted in terms of application potential due to in large part to its severely poor thermal stability – shown to undergo crystallization at temperatures as low as ~125ºC[23,31,35]. The low temperatures at which ITO experiences amorphous-to-crystalline transition has negatively impacted its implementation in multi-layered electronic devices due to the undesirable effects which phase transformation has on interfacial contact properties[59,60,65].

The recent inclusion of 10 wt. % Zn into In_2O_3-based (IZO) films has been shown to significantly improve the thermal stability of the amorphous-phase by delaying the onset-of-crystallization up to ~500ºC in ambient air environments[1,9,10,28,38]. Furthermore, *a*-IZO has been shown to possess both the highest reported carrier mobility (~50 cm^2/Vs)[1,2,9] as well as the highest TFT field effect mobility (~30 cm^2/Vs)[1,2,9,66] among other AOS materials. While IZO shows substantial application potential as a high-performance amorphous oxide, its naturally high carrier concentration in the as-deposited state (>10^{20} cm^{-3}) has prevented its use as a semiconducting material (<10^{17} cm^{-3})[15,28], subsequently reducing any chance for widespread commercial implementation.

To address IZO's intrinsically high carrier density, numerous IZO studies have attempted to uncover its underlying carrier mechanisms in order to suppress carrier generation whilst maintaining its other promising optoelectrical and microstructural characteristics. Recently, IZO's carrier concentration has been shown to exhibit the same

dependency as other In_2O_3-based thin films on the oxygen stoichiometry within the film[1,28,67]. The primary carrier doping mechanism associated with IZO is owed to the formation of native oxygen vacancy defects thin film growth[1,28,67], explained by the Kröger-Vink notated relationship of[1,28,67]:

$$O_O^X = \frac{1}{2} O_{2(g)} + V_{\ddot{O}} + 2e^- \quad (1)$$

where O_O^X represents an oxygen atom located on the oxygen sub-lattice, $V_{\ddot{O}}$ is a doubly-charged oxygen-vacancy which releases two free electrons, and $2e^-$ represents the two free electrons liberated by the formation of an oxygen vacancy[1]. Thus, as every present oxygen-vacancy is shown to donate two excess carriers, it can be stated that the carrier concentration of *a*-IZO is a direct function of the oxygen vacancy concentration within the film[1]. Therefore, strategies which aim to reduce oxygen vacancy generation show high potential for lowering IZO's carrier concentration to the semiconducting regime.

2.3 Conventional Doping Strategies of Indium-Oxide Materials

In recent years, the exponential growth of employing amorphous-G*a*-doped IZO (*a*-IGZO) as the channel layer material in flexible TFT applications[36,52] has attracted significant attention to the possibilities of utilizing alternative ternary-/quaternary-cation dopants for application[15,33,37,39,40,42-47] . The G*a*-doping of IZO has been shown to reduce the carrier density of *a*-IZO films fabricated under the same conditions from 10^{18} cm^{-3} to 10^{13} cm^{-3} while maintaining a drastically higher carrier mobility (>10 cm^2/Vs) in comparison to commonly-used *a*-Si:H (<1 cm^2/Vs)[1,8,9,15,18,22,33]. It is theorized that Ga possesses the capability to effectively suppress the formation of oxygen vacancies in IZO primarily due to its high ionic potential (+3 charge and small ionic radius)[15].

However, while *a*-IGZO shows great promise, and even has already been implemented for commercial use, *a*-IGZO TFTs' stabilities suffer greatly when subjected to thermal- and light-induced bias[15,68]. Thus, numerous studies investigating alternative ternary-cation dopant materials for IZO, including Si[33,34,37,42,43], Hf[44-47], and Ta[69,70], in attempts to provide a more stable doped-IZO compound while maintaining high performance characteristics.

In 2014, a comprehensive investigation of IZO doping strategies performed by Parthiban et al. established the guidelines for determining which materials may act as effective dopants in IZO TFTs[15]. Ultimately, seven interrelated material characteristics – electronegativity, ionic radius (r), effective core potential (Z_{eff}), Lewis acid strength (L), ionic dopant's size in relation to the host material's, carrier suppression capabilities, and metal-oxide bonding strength (M-O) – were discovered to dictate a dopant's potential for use in TFT applications[15]. Out of the seven parameters investigated, it was determined that L, Z_{eff}/r^2, and M-O are the primary material characteristics to consider when determining whether a material qualifies as a viable ternary-cation doping candidate. According to the study, materials with high L, Z_{eff}/r^2, and M-O are shown to effectively enhance the amorphous nature of the compound-IZO materials while acting as effective carrier suppressors with strong binding natures to IZO[15]. An element with a high L is believed to more effectively polarize the electronic charge away from oxygen 2p valence bands than those with weaker L values, resulting in increased levels of charge screening and, subsequently, higher carrier mobility values[15,71]. The Z_{eff}/r^2 value directly affects the L of a dopant material and is also believed to contribute to the stability of the amorphous-phase in doped-IZO films[15]. A high M-O bonding strength is directly

indicative of a ternary-cation's ability to suppress the formation of oxygen vacancies (and subsequently, free carriers) within due to an elevated attraction between the dopant material and oxygen ions[1,15]. In Table 2.1, the Lewis acid strengths, Z_{eff}/r^2 values, and M-O bonding strengths of heavily investigated ternary-cation dopants, as well as minimally investigated Al^{3+} (only one other notable study prior to this thesis)[72], may be observed.

Table 2.1. Lewis acid strengths (L), Z_{eff}/r^2, metal-oxide bonding strengths (M-O), and ionic radii (r) of established *a*-In_2O_3-dopants[15,73].

Cation	L	Z_{eff}/r^2	M-O (kJ/mol)	r (pm)
Ga^{3+}	1.167	5.194	353.5	187
Hf^{2+}	1.462	5.536	801.7	225
Si^{2+}	8.096	13.717	799.6	210
Al^{3+}	3.042	6.584	511.0	184
In^{3+}	-	-	-	220

It is apparent through the characteristics presented in Table 2.1 that Al^{3+} holds credibility as a potential ternary-cation dopant in *a*-IZO films due to its relatively high L (only Si is greater), as well its excellent M-O bonding strength (>M-O of commonly-used Ga)[15,73]. Furthermore, Al^{3+} fits the ionic radius requirement for viable IZO-dopants as the ionic radius of Al^{3+} (184 pm) is smaller than In^{3+} (220 pm)[73]– indicating that there is low probability for an increased formation of defects to occur when Al^{3+}-doping IZO host materials.

2.4 Previous Aluminum-Doped IZO Findings

While previous studies have included the use of aluminum in IZO applications, such as the utilization of AlO_x as a passivation layer in AT-IZO TFTs[4], many of the prior investigations cannot provide direct and comparable insight into Al^{3+}'s carrier suppression effectiveness as a ternary-cation dopant in IZO.

However, in 2010, Sun et al. conducted an initial study into the effects of Al^{3+}-doping *a*-IZO thin films via co-sputter deposition[72]. Using a similar approach to that of this study's, the investigation deposited Al^{3+}-doped IZO through a co-sputter technique where IZO power was held constant at 60W (RF) with increasing Al^{3+} deposition powers (RF) at 0W, 1W, 4W, 7W, 9W, 11W, and 16W[72]. Unfortunately, the 2010 study presented their selected deposition intensities only as plasma power (W) - instead of plasma power density (W/cm^3) – and did not provide the material target sizes used, making both sample and analysis replication unattainable[72]. Furthermore, instead of using pre-determined deposition rates to grow films of the same thickness, the study deposited every sample at a set time period of 2hr[72]. No sample thickness values are provided, leading to valid concerns of accurate trend examination across increasing dopant-power depositions. A key worry prior to even observing the published results and subsequent analysis is the possibility of bulk film fabrication at higher deposition powers (in lieu of thin films). Bulk oxide compounds have been shown to possess drastically different properties than that of their thin film compound counterparts[74] and with the combination of no reported film thicknesses and a constant deposition period across all samples[72], bulk oxide formation throughout this study is of major concern. When examining the microstructural data of the study, it is claimed by the researchers that a formation of Al_2O_3 nanocrystallites occurs when Al^{3+} is doped into an IZO thin film matrix[72]. However, it is widely accepted that the appearance of any non-In_2O_3 XRD peaks in ternary-doped In_2O_3-based oxides is highly improbable (excluding those with excessive dopant wt. %) and thus, the crystallization of Al_2O_3-paramorphs is questionable at best[72]. Furthermore, at Al^{3+} deposition powers >7W, the acquired resistivities of the IAZO samples drop significantly (almost to that of

the pure-IZO samples)[72] which is in direct contrast to the Al^{3+}-doping expectations produced by its potential ternary-cation dopant effectiveness in Section 2.2.

Though the previously-discussed investigation claims may be questionable, the lack of supplementary Al^{3+}-doped IZO thin film studies prevents further criticism as no additional literature is available to for a valid cross-examination. Therefore, one cannot completely dismiss the assertions made in the 2010 study, as it is one of the few, if not only, Al^{3+}-doped IZO thin film studies available to the public.

CHAPTER THREE

Experimental Methodology

3.1 Fabrication of Al^{3+}-Doped Indium Zinc Oxide Thin Films

In order to effectively fabricate Al^{3+}-doped *a*-IZO thin films, a dual co-sputter technique was implemented using a UHV K-Lab sputter deposition system. Sputter deposition, one of the many physical vapor deposition techniques available, involves the combining of the introduction of a controlled gas into a vacuum chamber while electrically energizing a cathode in order to generate plasma[75]. Prior to plasma initiation, a target material is firmly clamped to the exposed surface of the cathode in order to "grow" a thin film on a desired substrate material. Gaseous atoms lose electrons inside the plasma in order to become positively charged ions which then bombard the target, providing enough kinetic energy to remove material atoms and generate a vaporized material stream which traverses the chamber and deposits onto a substrate material (microscope glass slides and/or Si wafers in this study)[75]. In the case of the co-sputter deposition technique, multiple target materials may be clamped to separate cathodes which are then ignited at the same time in order to deposit a multi-material thin film. In sputter deposition processes, UHV level ($<5.0 \cdot 10^{-5}$ Torr) is required in order to prevent unwanted airborne contaminants from mixing with the sputter gas which may in turn affect the resulting properties of the deposited thin films. UHV is achieved through implementation of a series of two pumps: (i) standard rotary pump in order to achieve vacuum level pressures of $<5.0 \cdot 10^{-3}$ Torr and

(ii) a turbo-pump which allows for the chamber to then attain vacuum pressures of down to ~$2 \cdot 10^{-7}$ Torr.

3.1.1 The Roles of Sputter Deposition Chamber Parameters

Several chamber parameters play crucial roles in the electrical, optical, and structural properties of sputter-deposited thin films, such as base pressure (Torr), working pressure (Torr), target-to-substrate (T-s) distance (mm), plasma power density (W/cm^3), power type (DC or RF), deposition time (s), pre-sputter deposition time (s), and substrate rotation (rpm). A computerized control panel embedded into the sputter deposition system allows for user control of all the major deposition- influencing settings.

Base pressure is defined as the vacuum level of the chamber prior to sputter-deposition and is desired to be set at the lowest possible pressure in order to, as stated before, remove the possibility of airborne contaminants mixing with the sputter gas which may affect the resulting thin films. For base pressure requirements, <5.0e-5 Torr is deemed suitable as the amount of present airborne contaminants can be said to be negligible at this level of vacuum. Working pressure is termed as the pressure of the deposition chamber during the fabrication process, controlled by two separate parameters: (i) Sputter gas input level (sccm) and throttle-valve (T/V) opened/closed percentage (%). Sputter gas input is regulated through varying the flow level (sccm) of either the pure Argon (Ar) tank connected to the system, the mixed 80% Ar/ 20% Oxygen (O_2) tank, or both. Ar is the only sputter gas used throughout this study. The T/V connects the main chamber to the rotary and turbo pump line, where its position is easily controlled through altering the valve's settings. The T/V can be set to be fully open (100%, high vacuum/low pressure), fully closed (0%, low vacuum/high pressure), or somewhere in between (depending on the

desired position). T-s distance plays a strong role in both the outcome of the deposition, depending on the material used, and the length of the deposition in terms of time.

T-s distance, or target-to-substrate distance (as mentioned before), is defined as the overall distance between the center of the target material (on the exposed surface) and the substrate placed in the chamber. As T-s distance increases, the deposition rate (nm/s) has been shown to decrease, resulting in an indirectly proportional trend. Furthermore, an increased T-s distance may result in weaker adhesion between the deposited thin film and the substrate material (glass or Si wafers), resulting in an overall decrease in surface uniformity. Substrate rotation plays a vital role concerning the final depositions' surface roughness and uniformity, as a rotating substrate platform prevents uneven growth of the target material. Too fast of a rotation setting may exhibit the same issues as no rotation and thus, an optimal setting must be determined in order to verify film surface uniformity across all substrates present in the chamber.

Plasma power density is, as its name implies, the total amount of power applied to the target material over the volume of the target itself. Both the type (DC or RF) and intensity of the power applied to the target (DC or RF) play a substantial role in the outcome of the deposition process. DC sputtering is known as the most basic and inexpensive form of sputtering, primarily used when depositing metallic or electrically conductive target materials[76]. The primary limitation with DC sputtering concerns the deposition of non-conducting, insulating materials, which are known to build up charge on the surface of the target material over time in the case of DC sputter, resulting in an arc-like erosion of the material (arcing) and/or contamination of the surface[76]. RF sputtering mitigates the issues that arise with non-conductive DC sputtering by alternating the electrical potential

of the current in order to avoid charge buildup[77]. However, due to use the of radio waves instead of DC current, RF sputtering suffers from much slower deposition rates, leading to an increased length of deposition time to achieve the same thickness of a DC-power deposited film[77]. This increased deposition time raises the costs of fabrication substantially, therefore, in the case of conductive target materials, DC sputtering is said to be the preferred method of deposition. The level of power applied to the material (for both DC and RF) plays a crucial role in both the processing and final parameters of deposited thin films, such as the deposition rate, electrical characteristics, optical properties, film microstructure, and film uniformity. Both the optimal deposition power type (DC or RF) and power level for a target material may vary depending on the chemical composition of the material and must be iteratively determined in order to discover the best power settings in order to produce a thin film with the desired properties. The overall length of time of the deposition, as one may assume, dictates the resulting thickness of the deposited film. Film thickness is an important parameter when concerning the fabrication of thin films, as too thick of a grown film may result in both a decrease in overall transparency in the visible spectrum and additional carrier scattering mechanisms in certain semiconducting applications (such as channel layer implementation). Film transparency is a vital parameter when concerning applications which require ambient and visible light to pass through the thin film, such as solar cell and display device applications. Thus, developing films which possess desirable electrical properties whilst remaining transparent in the visible makes film thickness a crucial parameter. Furthermore, consistently fabricating similar in thickness thin films is vital in order to effectively compare the analysis results among different samples, such as transmittance in the visible regime, microstructural properties,

and electrical performance parameters. Pre-sputter deposition is a required deposition process, involving the sputtering of the target material prior to opening the main shutter in the chamber, removing all contaminants from the targets, themselves. Length of time of the pre-sputter process varies based on the target material in question, as certain materials are more prone than others to bonding with certain chemicals in air, such as Al^{3+}, which naturally develops a thin Al_2O_3 protective coating layer on the surface due to ambient exposure. Al^{3+} by itself is a conducting metallic material, where Al_2O_3 is a wide band gap insulating material with drastically different electrical, optical, and structural properties than Al^{3+}.

In summary, both prior to and during the fabrication processes, there are many parameters which strongly influence the resulting fabricated films, and all must be considered and thoroughly investigated when depositing the desired material. In most cases, iterative deposition processes which consist of altering one variable at a time are required in order to determine the optimal parameters for each material, depending on its potential applications.

3.1.2 Sputter Parameter Selection for Highly-Conductive Indium Zinc Oxide

When approaching the Al^{3+}-doping process of *a*-IZO, the first and most crucial fabrication parameters concern developing the highest conducting *a*-IZO film as possible. While there are semiconducting applications for *a*-IZO, synthesizing highly conductive (low ρ) films allows for simple and easy analysis of the thin films at hand. Using a 99.9% pure-IZO target (90 wt. % In_2O_3: 10 wt. % ZnO), provided via K-Lab, Korea, while also utilizing both reference literature and iterative manufacturing steps, the sputter deposition

machine's parameters which produced the highest possible conducting *a*-IZO film were determined ($\rho \approx 2.74e\text{-}3\ \Omega\text{-cm}$).

The pre-sputter time required to remove contaminant particles from the *a*-IZO material was relatively short in length, at 5 minutes for the first deposition of the series and 30 seconds for all depositions following. Once the first pre-sputter deposition is completed, contaminants which may affect the deposition outcome are completely removed from the vacuum chamber and target material. The decreased subsequent pre-sputter times not only allow for more deposition processes to be completed in the same time interval but also further preserve the remaining target material which has yet to be vaporized, extending the lifespan of the costly substance. The overall time of the deposition was found through iterative processes, as deposition power also affects the rate of deposition growth, aiming for a film thickness of ~100 nm. For a ~100 nm thick *a*-IZO film at 25W (DC), the time required is 1550s.

Concerning base pressure, as stated prior, depositions were performed once the main chamber achieved a vacuum level of $<5.0 \cdot 10^{-5}$ Torr. The base pressure setting ensures that all aerosol-contaminants introduced to the chamber during the target and substrate loading processes are negligible in quantity and will not affect the resulting films. The optimal working pressure level found through iterative deposition processes, alike the majority of the other deposition settings. At first, depositions at 15sccm (Ar) and a 35% T/V position were conducted, resulting in a working pressure of $2.0 \cdot 10^{-3}$ Torr. However, later on in the study, it was discovered that in comparison to higher sccm values, 15 sccm resulted in less reliable and more inconsistent fabricated films, varying both the electrical parameters and resulting thicknesses too often for trustworthy results. The error in repeated

depositions was attributed to a lack of consistent Ar flow throughout the chamber, potentially not allowing for proper bombardment of material onto the glass and Si substrates. Thus, in order to mitigate the issue of inconsistent depositions, the Ar sccm level was set at 30 sccm and the T/V position was set to full-open (100%), resulting in a working pressure of $2.1 \cdot 10^{-3}$ Torr. The $0.1 \cdot 10^{-3}$ Torr pressure difference was deemed negligible in terms of affecting the properties of the resulting films.

As the *a*-IZO target is a conductive material, DC power was used in order to not only accelerate the growth of the film generated but also to ensure that the majority of the doped-films' composition was primarily *a*-IZO (utilizing RF power for the Al^{3+} target in order to slow down the rate of Al^{3+} growth in the multi-material film). After several iterative processes, DC 25W was chosen to minimize the plasma power density, removing the possibility of substrate damage caused by too intense of a DC plasma stream, while still guaranteeing uniform and consistent film growth. At a working pressure of $2.1 \cdot 10^{-3}$ Torr, the voltage and current parameters required to obtain 25W were 304 V and .082 A, respectively. It was found that as working pressure increase, the voltage of the deposition decreases in parallel with the overall conductivity of the film.

The T-s distance that was selected for *a*-IZO film growth was 85.7 mm, discovered once again through iterative processes and controlled via the substrate Z-height parameter of 70 mm. Too large of a T-s distance was found to result in a substantial increase of deposition time, along with a negative impact on the film's overall uniformity and deposition consistency. Closer than 85.7 mm had little-to-no effect on the overall deposition of the *a*-IZO film, and thus was chosen as the substrate being too close to the plasma plume may result in high-energy damage to the film surface. The substrate rotation

for the *a*-IZO deposition was set to 5 RPM in order to guarantee uniform deposition growth across the substrates. As stated before, both too fast and too slow of rotation may cause inconsistencies in surface roughness and result in varying thin film height across the surface of a substrate. Thus, through iterative processes, 5 rpm was selected to be the optimal rotation for the deposition with all other parameters kept in mind.

Overall, after finding a basis for conductive *a*-IZO deposition parameters from previous literature and iteratively tweaking the deposition variables one-by-one, the highest conductivity *a*-IZO depositions settings were found, resulting in low resistivity of ~$3 \cdot 10^{-}$ Ω-cm. Once the *a*-IZO deposition parameters were narrowed down, the aluminum doping processes could proceed.

3.1.3 Sputter Parameter Selection for Al^{3+}-Doped Indium Zinc Oxide

To effectively determine the effects of Al^{3+}-doping *a*-IZO via co-sputter deposition, incrementally varying the amount of aluminum present in the doped-IZO film was instrumental. Prior to the doping processes, it was decided that RF power was to be used for the Al^{3+} target in order to guarantee that less Al^{3+} was present in the film than *a*-IZO due to the slower deposition rate of RF power.

First, the pre-sputter settings for the Al^{3+} target were investigated in order to determine how much time was necessary to remove any contaminants (primarily Al_2O_3) form the material itself. Originally, it was deemed that >600s (10min) was an appropriate time to remove the contaminants from the material and obtain a pure Al^{3+} dopant in the doped-IZO samples. As power settings of <10W on the RF guns proved to produce unstable, discontinuous plasma streams, the RF power was varied from 10W to 25W in increments of 5W. Originally, the Al^{3+}-doped *a*-IZO samples exhibited reliable results

throughout fabrication but unfortunately, did not produce data which were consistent with what the results theorized from prior-literature suggested. After some time, the analysis was initially concluded to be accurate, even if unpredictable. However, it was later uncovered during a repeated deposition that a pre-sputter length >1hr produced drastically different results than the previously fabricated samples. Not only did the new, longer pre-sputter parameters contribute to the production of samples which followed the theorized trends, the films exhibited characteristics showing high potential for Al^{3+}-doped *a*-IZO future application. Thus, it was decided that, moving forward, >1hr of pre-sputter time would be the required pre-sputter time setting for IAZO film fabrication.

As previously stated, in order to obtain a holistic understanding of the effects of Al^{3+}-doped *a*-IZO, incrementally increasing the dopant percentage in the IAZO films was crucial, obtained via altering the RF power at which the aluminum target was deposited. Since the co-sputter technique for the ternary-cation doping of *a*-IZO is a relatively novel method (in comparison to synthesizing single *a*-IZO-doped targets), iterative deposition steps, similar to those performed for sputter parameter discovery, were performed in order to get a baseline of the necessary RF power required for Al^{3+}-doping. At first, a baseline maximum RF power needed to be found in order to guarantee that all samples moving forward possessed transparency parameters which allowed the samples' thicknesses to be measured by an ellipsometer. At the time of fabrication, analysis methods which could measure nanometer-scale opaque/non-transparent films such as SEM or AFM techniques were not available. Thus, ensuring that the highest-doped IAZO film possessed the substantial transparency in order to be analyzed properly was instrumental to obtain valid data for comparison. After several iterative tests, it was revealed that 25W (RF) was the

highest Al^{3+} deposition power used which would produce visibly transparent IAZO films. From there, recalling that 10W was the lowest RF power which would maintain a steady plasma stream for aluminum, the power was incrementally decreased by 5W to obtain five separate sample sets with varying amounts of doping material in the films (as-deposited *a*-IZO, 10W, 15W, 20W, and 25W).

3.1.4 IAZO Post-Fabrication Treatment

In order to effectively analyze the Al^{3+}-doped *a*-IZO films in comparison to standard *a*-IZO films, it is desired to study the effects of simple post-fabrication air-annealing at temperatures up to 500ºC. *a*-IZO has shown remarkable stability in the amorphous-phase in ambient air conditions at temperatures up to 500ºC where, as mentioned before, *a*-IZO undergoes crystallization[1,9,10,28,38]. Furthermore, ambient-air annealing has been determined as a practical technique used to implement controllable carrier suppression allowing for potential semiconductor applications[27,41]. Thus, studying how the IAZO samples respond to increased annealing temperatures, varying from 100ºC to 500ºC in intervals of 100ºC, should allow for valuable insight into how Al^{3+}-doping may affect *a* -IZO's response to air-annealing.

To reliably acquire annealing temperature data, minimization of the contact resistance between the data acquisition probes and the thin films is necessary. When dealing with low-resistance electrical measurements, the formation of contact resistance between metal oxide sample films (IAZO) and the gold-plated data acquisition probes may result in inaccurate and inconsistent readings, prohibiting proper analysis of the films' responses to annealing temperature variation. However, through sputtering a non-reactive metallic coating to the contact points on the IAZO film, metal-to-metal contact may be

established. It is crucial that the material used for contact metallization be non-reactive with *a*-IZO in order to preserve the integrity of annealing temperature analysis, as it has been shown that an *a*-IZO-reactive material, such as Ti, may inject carriers into the host material when introduced to elevated temperatures[31,78], skewing the resulting data. Molybdenum (Mo) has been shown to have negligible effects on the electrical properties of *a*-IZO even throughout post-fabrication annealing exposure[31] and, subsequently, was selected as the candidate material for contact metallization. By placing a patterning shadow-mask on top of the already-deposited IAZO thin film, as seen in Figure 3.1, each exposed corner of the sample was layered with a Mo film, allowing for metal-to-metal

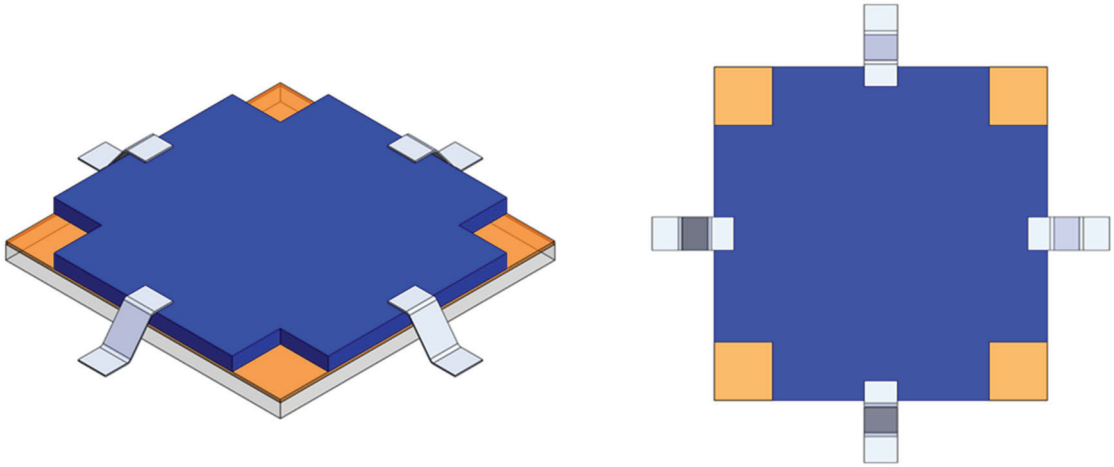

Figure 3.1. An (a) isometric and (b) top view of the patterning-process used to metallize the four corners of each sample. The top layer (blue) is shadow-mask, designed to allow deposition exposure to the four corners of a thin film-coated glass slide, held in place with four pieces of temperature-resistant tape.

contact between the probes and the sample without skewing the measurements. As the corner-patterns generated did not require exact precision, the shadow-mask was secured to

the sample via heat-resistant Teflon tape and did not necessitate the use of a shadow-mask aligner.

The IAZO samples were air-annealed on a hot plate capable of reaching a maximum temperature of 550ºC. The samples were first placed on top of a standard glass microscope slide to avoid direct contact with the aluminum foil wrapping around the hot plate (for sanitary purposes) and then covered with an empty 500 mL glass beaker to simulate an ambient-air annealing environment while also eliminating any skewed results from inconsistent drafts within the room. As previously stated, both IAZO and *a*-IZO samples were air-annealed at temperatures of 500ºC for ~1hr. Due to the time-sensitive rate reaction between the oxygen available in the air and the oxygen vacancies present in *a*-IZO, discussed in Chapter 2, the annealing time was monitored closely in order to acquire consistent and comparable data.

3.2 Thin Film Analysis of IAZO Films

When investigating transparent thin films, the primary basis for deciding which analysis techniques to use relies on the potential applications of the material. Concerning IZO, the primary thin films properties which must be investigated may be sectioned into three groups: electrical, optical, and microstructural. In many cases, various parameters from each of these groups may be related to a parameter in another, yet the analysis techniques are separated due to the dat*a*-collection methods involved. For the electrical properties, the important parameters which were investigated in this study are carrier concentration, carrier mobility, and resistivity. Concerning the optical parameters, the two major characteristics looked at were the transmittance of the films and the resulting optical band gaps. The microstructural data desired for publication, such as x-ray diffractometry,

scanning electron spectroscopy (SEM), and atomic force microscopy (AFM) was partially collected, as only XRD data was obtained. AFM/SEM analysis was not performed due to the time constraints of the study and the equipment readily accessible to the researchers. This section details the experimental methods taken to obtain the thin film data presented and also provides some background theory and motivation for implementing these techniques.

3.2.1 Electrical Analysis

The first step one must take in order to properly analyze IAZO involves the full characterization of the films' resistivities. Resistivity information is used to establish that the deposition conditions used to produce the baseline *a*-IZO films are consistent with prior research as well as being used to accurately determine how incrementally increasing the amount of Al^{3+}-dopant in *a*-IZO films affects electrical performance. Two separate methods were utilized to collect resistivity data: (i) the four-point probe technique and (ii) the Van der Pauw resistivity method. The incorporation of both analysis techniques was performed in order to verify the accuracy of the measurements (acceptable error was deemed +/- 10%).

Both resistivity methods require the use of an ellipsometer to measure the thickness of the films. Individually, these methods obtain the sheet resistance of the fabricated thin films fabricated which in turn may be converted to resistivity through[79]:

$$\rho = R_S \times t \tag{2}$$

where ρ is film resistivity (Ω-cm), R_S is sheet resistance ($\Omega/\square$), and t is the thickness of the film (nm). As one may infer, low-error thickness measurements are vitally important in

order to obtain consistent and comparable resistivity values across the films analyzed. Access to the Film Sense FS-1 Multi-Wavelength ellipsometer provided the capability to measure the thin film thicknesses with an accuracy of <2.7 nm and a precision of <.05 nm on films up to 500 nm thick[3]. The high-precision/-accuracy capabilities of the FS-1 ellipsometer allow for trustworthy evaluations of the films' thicknesses, and in turn resistivities, mobilities, and carrier densities by eliminating any possibilities of substantial error.

The first method used to acquire resistivity, the four-point probe technique, as its name implies, utilizes four equally-spaced probes to determine the sheet resistance of a thin film. The voltage is measured across the two interior probes while a power source provides a current flow between the two outer probes. Low resistivity films are preferred for the four-point probe technique, as ideally the probes will make ohmic contact with the film involved and not skew the measurement due to the formation of a metal-to-semiconductor Schottky barrier[80]. In Figure 3.2, a rendering of the interaction between the four-point probe tool and a thin film samples may be observed. As seen, a current source (I) is introduced to probe 1 and is drained by probe 4, where the potential difference (V) is extracted from probes 3 and 4. As the sample may be assumed to be an infinite sheet[80], the sheet resistance, R_S (Ω/□) may be defined as:

$$R_S = \frac{\pi}{\ln(2)} \frac{V}{I} \tag{3}$$

where V is the voltage potential across probes 2 and 3 (V), I is current (A), and $\frac{\pi}{\ln(2)}$ is the geometric factor which accounts for the infinite sheet logarithmic assumption[80].

An alternative method for determining the sheet resistance of a thin film is through the implementation of the Van der Pauw resistivity method. The Van der Pauw resistivity

method is based on the premise that, in an ideal situation, the sheet resistance across one edge of a square-shaped sample should be equal (or close) to both the sheet resistances of the other edges[79]. Thus, an averaging of the sheet resistances measured across all edges should work to minimize the error involved with obtaining resistance data. Additionally, the reversed polarity method utilized in this study further improves the exactness of the resistance values gathered via repeating the measurements after flipping the polarity of the current source.

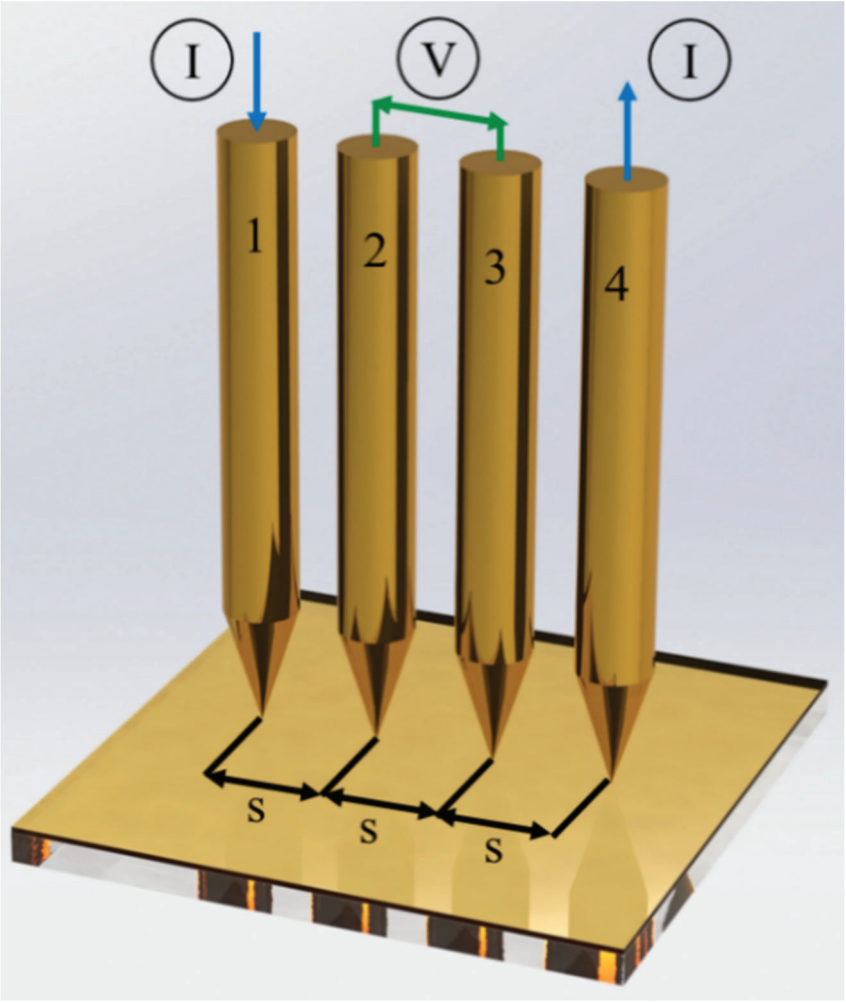

Figure 3.2 Three-dimensional model of a four-point probe designed to obtain the sheet resistance (Ω/□) of a thin film. Directly under the four probes in the figure is a model of a typical thin film sample, placed for reference and visual aid.

By measuring the sheet resistance of each edge twice (reversing current flow for both edges) and averaging through an iterative numerical process provided by the National Institute of Standards and Technology (NIST), the Van der Pauw technique allows one to obtain precise sheet resistance measurements with low overall error.

As can be seen in Figure 3.3, the resistance measurements are taken across the four edges, where the dotted arrows indicate the direction of current flow during the measurements. As one may infer, R_{14} indicates the sheet resistance measured across the edge connecting points 1 and 4 with the current being sourced through point 1 and drained through point 4.

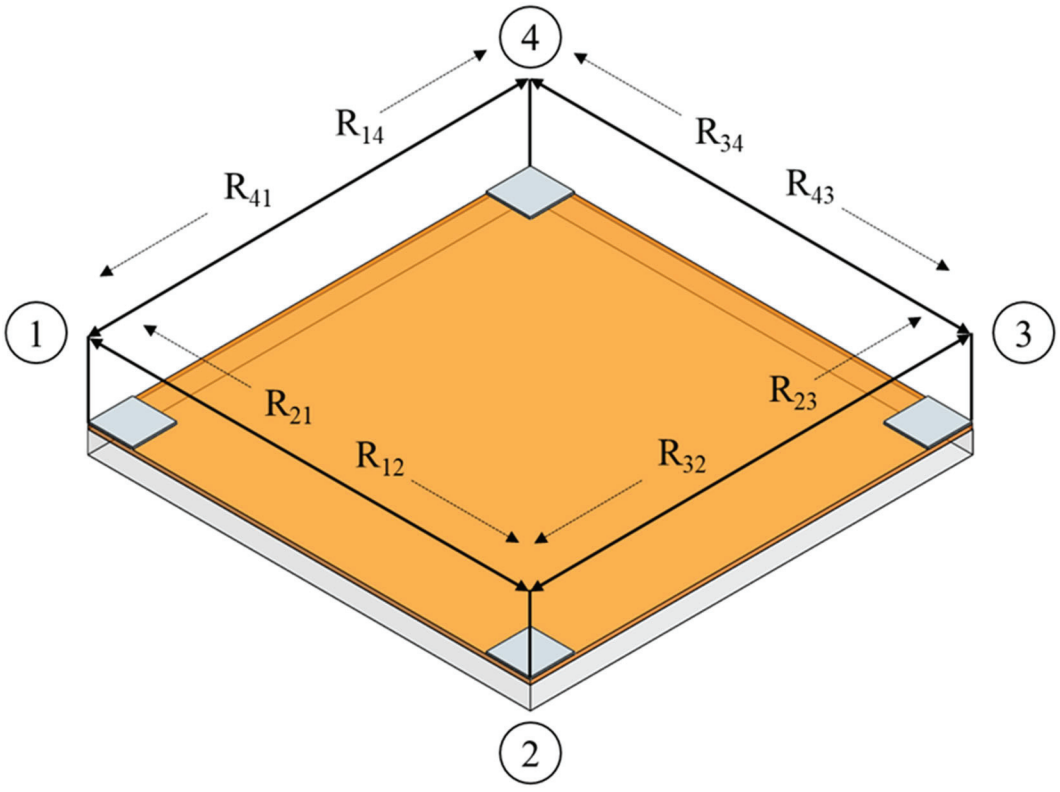

Figure 3.3. Three-dimensional model of a corner-contact-metallized thin film sample, visualizing where measurements are taken and the inlet/outlets of the current flow.

While the current is flowing through two separate points, the voltage on the opposite edge is measured and recorded (i.e. V_{12} when I_{34} is flowing) and, when used in combination with Ohm's Law, the sheet resistance may be extracted through:

$$R_{I34,V12} = \frac{V_{12}}{I_{34}} \tag{4}$$

where $R_{I34,V12}$ is the sheet resistance of the sample calculated via sourcing current through probe 3 to probe 4, I_{34}, and the voltage across probes 1 and 2 is defined as V_{12}. These measurements are repeated for all edges (twice to account for polarity), and separated into vertical sheet resistance, R_v, and horizontal sheet resistance, R_h, which are defined by[79]:

$$R_v = \frac{R_{21,34} + R_{12,43} + R_{43,12} + R_{34,21}}{4} \tag{5}$$

$$R_h = \frac{R_{32,41} + R_{23,14} + R_{14,23} + R_{41,32}}{4} \tag{6}$$

where R_v and R_h are then used to solve for R_S numerically, as seen in the next set of equations. The Van der Pauw equation for the sheet resistance is defined by[79]:

$$\exp\left(\frac{-\pi R_y}{R_S}\right) + \exp\left(\frac{-\pi R_h}{R_S}\right) = 1 \tag{7}$$

which can be solved via the iterative steps below, provided by NIST[79]:

(1) Set the error limit, δ, to 0.0005, corresponding to 0.05%

(2) Calculate the initial value of z_i, z_o:

$$z_o = \frac{2 \ln 2}{\pi(R_v + R_h)} \tag{8}$$

(3) Calculate the ith iteration of y_i:

$$y_i = \frac{1}{\exp(\pi z_{i-1} R_y)} + \frac{1}{\exp(\pi z_{i-1} R_h)} \tag{9}$$

(4) Calculate the ith iteration of z_i where:

$$z_i = z_{i-1} - \frac{(1 - z_i)/\pi}{\frac{R_v}{\exp(\pi z_{i-1} R_v)} + \frac{R_h}{\exp(\pi z_{i-1} R_h)}} \tag{10}$$

(5) When $(z_i - z_i\text{-}1)/z_i < \delta$, stop iterations and calculate:

$$R_S = \frac{1}{z_i} \tag{11}$$

Following the aforementioned steps allows for the precise calculation of the material's sheet resistance and ensures that the error involved with the source measurements is <0.05%.

To properly execute the Van der Pauw method for resistivity, the versatility of the Keithley 4200-SCS Semiconductor Characterization System, seen in Figure 3.4, is utilized. The same Keithley machine may also be used to gather carrier transport values, which is discussed in further detail within the following section. The Keithley 4200-SCS Semiconductor Characterization System is a programmable data acquisition instrument designed for electrical property analysis which, in this study, requires four separate source measure units (SMUs). The SMUs, seen in Figure 3.4, allow for the Keithley system to accurately source and measure voltage and/or current, both individually or simultaneously depending on the application and number of SMUs available. The SMUs are programmed through the Keithley 4200-SCS to source current, drain current, and measure the potential difference (voltage) between two probes. For example, to obtain $R_{21,34}$, SMU 2 provides a series of source current (10 steps, i.e. 10 measurements of the same current), SMU 1 drains the current while simultaneously logging the current through (should be near-equal to

source current but measured for calculations and verification that there is not a short), and the potential difference is measured across SMUs 3 and 4.

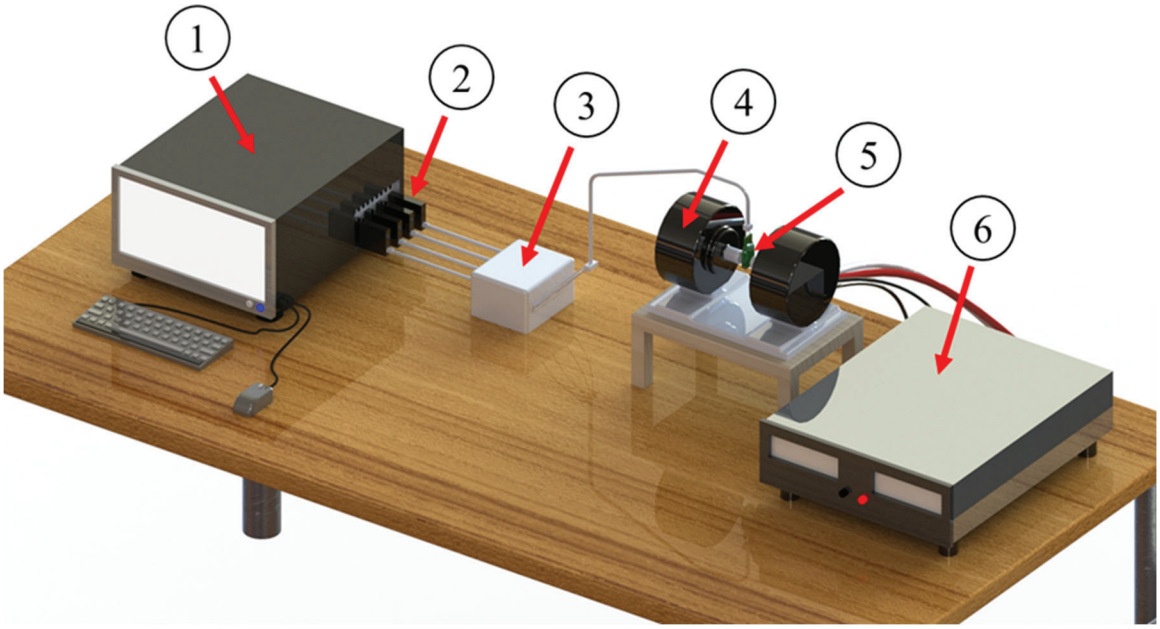

Figure 3.4. Graphical visualization of the system designed, built, and implemented to collect Hall Effect data as well as verify four-point probe resistivity measurements. Instrument 1 (I1) in the figure is the Keithley 4200-SCS Semiconductor Characterization System, where Keithley-provided software (Keithley Interactive Test Environment) is programmed by the user to collect specific data. I2 labels the four low-error DC source-measure units (SMUs), which provide applied currents/voltages to I3, a custom cable-converter fabricated for the integration of I1 and I2 with an internally-wired plastic-mount (I5) to analyze fabricated thin films. I5 may be observed and is further detailed in Fig. 3.5. I4 is the high-field tabletop electromagnet, which is powered by I6, the high voltage/current power supply. Electromagnet water-cooling system not shown.

The sample holder, which is the interface between the SMUs and the sample itself, seen first in Figure 3.4 (I5) and in more detail in Figure 3.5. The coaxial cables connected to the SMUs are soldered to standard electrical wires in the cable converter box, seen in Figure 3.4, which in turn possesses four outlet cables soldered directly to the sample holder. The custom-built cable converter eliminates the need to directly solder the SMU coaxial

cables to the sample holder, allowing for the possibility of linking other data acquisition devices to the Keithley SCS-4200 Semiconductor Characterization System.

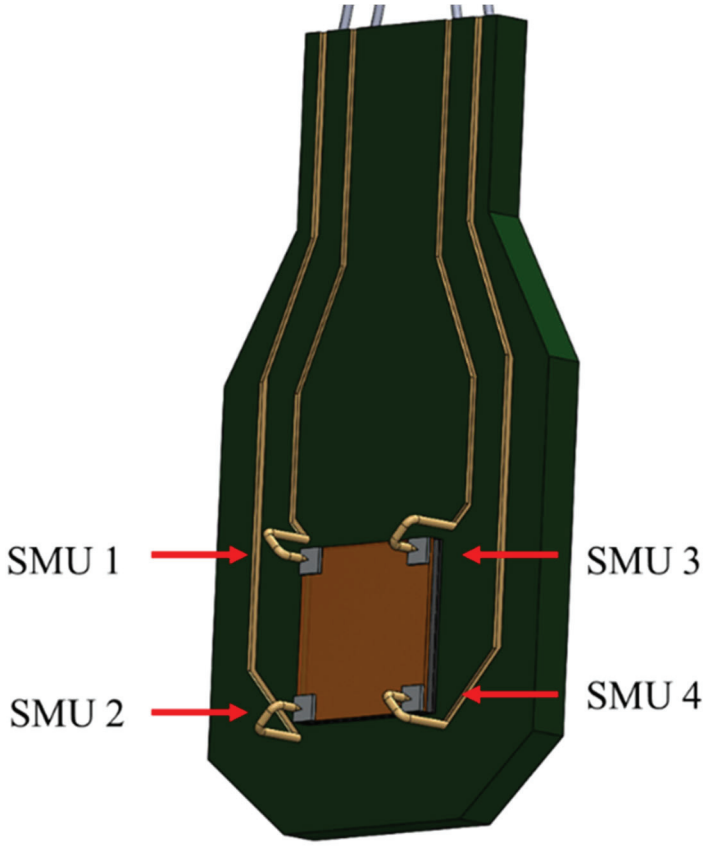

Figure 3.5. General rendering of the thin film sample holder and probe station utilized in the Hall Effect system (I5 in Fig. 3.4). The gold-plated internal-wiring from the four probes is extruded for visualization's sake, displaying how each probe relays output/input signals from the sample to its respective SMU. The thin film sample in this figure may be seen in further detail in Fig. 3.3.

As IAZO and *a*-IZO are conductive in their as-deposited states, the source current programmed should not be too low (~10e-9 A range), as the low resistivities of the material, via Ohm's law, would then generate low voltage readings causing minor inconsistencies/error to significantly affect the final data. However, the source current should also not be set at too high of a setting (~10e-3 A range) as any semi-conductive samples will be subject to charge buildup. Thus, it was determined that a middle-ground

of 10e-6 A would be sufficient for both the conductive and semi-conductive films fabricated. Resistivity measurements were taken for all samples, allowing for the thorough comparison of the Al^{3+}-doped samples with pure-IZO.

In order to determine the Al^{3+}-doping effects on *a*-IZO's majority carrier characteristics (mobility/concentration), the Hall Effect method was employed. The Hall Effect method allows for the precise, experimental measurement of both the majority carrier concentration of a semiconducting material and the major carrier mobility. To properly execute the Hall Effect method for semiconducting thin films, an integrated system roughly modeled in Figure 3.4 - consisting primarily of a Keithley SCS-4200 Semiconductor Characterization System (I1), a thin film sample holder (seen in Figure 3.5), and a high-field tabletop electromagnet - was utilized.

To better understand how the integrated system seen in Figure 3.4 collects the necessary data for thin film analysis, the underlying theory of the Hall Effect and its relation to the desired thin properties must first be explained. According to the NIST, the primary mechanism which drives the Hall Effect is the Lorentz force, a combination of an electric force and a magnetic force[81]. An electron travelling across an electric field perpendicular to an applied magnetic field experiences a magnetic force, F_M, acting normal to both directions, defined as[81]:

$$F_M = -q(v \times B) \tag{12}$$

where q is the elementary charge of an electron (1.602×10^{-19} C), v is the particle velocity, and B is the magnetic field. When accounting for the effects of the electric field, the resulting Lorentz force, F_L, may be defined as[81]:

$$F_L = -q(E + v \times B) \tag{13}$$

where E is the applied electric field. For n-type conductors such as IZO, where electrons are the known primary charge carrier (in comparison to p-type where holes are primary carriers), when an applied current flows across the thin film surface, e.g. from contact corner-point 1 to 2 in Figure 3.3, the electrons subject to F_L initially drift away from the current direction, resulting in an excess negative surface electrical charge on the original side of the sample[81]. The excess charge induces a potential drop across the two sides of the sample, which may be defined as the Hall Voltage (V_H)[81]. The magnitude of V_H is then utilized in the acquiring of a thin film sample's carrier concentration, n (cm^{-3}), through[81]:

$$n = \frac{IB}{qt|V_H|} \tag{14}$$

where I is the applied current (A), B is the magnetic field (G), q is the elementary charge (C), and t is the thickness of the thin film layer (nm). Subsequently, once n is obtained, the Hall mobility of an n-type thin film, μ_n (cm^2/Vs), may be determined via[81]:

$$\mu_n = \frac{1}{qn\rho} \tag{15}$$

where q is the elementary charge (C), n is the carrier concentration/density (cm^{-3}), and ρ is the resistivity of the film (Ω-cm), previously acquired via the four-point probe method and/or the Van der Pauw technique.

Similar to the iterative method detailed in Section 3.2.1 used to determine the sheet resistance of a sample, the NIST provides a comprehensive and straightforward method for determining Hall properties of a thin film. Thus, according to the NIST, the method for Hall Effect measured is[81]:

(1) Apply a positive magnetic field B (denoted by P in Hall voltage subscripts)

(2) Source a current across contact points 1 and 3 seen in Figure 3.3, I_{13}, and measure the voltage across contact points 2 and 4, V_{24P}

(3) Reverse the current (I_{31}) and measure voltage across contact points V_{42P}

(4) Repeat for V_{13P} and V_{31P} with I_{42} and I_{24}, respectively

(5) Reverse the magnetic field B (denoted by N in Hall voltage subscripts)

(6) Repeat steps II-IV to obtain V_{24N}, V_{42N}, V_{13N}, and V_{31N}

(7) Once voltage values are obtained, calculate the following:

$$V_C = V_{24P} - V_{24N} \tag{16}$$

$$V_D = V_{42P} - V_{42N} \tag{17}$$

$$V_E = V_{13P} - V_{13N} \tag{18}$$

$$V_F = V_{31P} - V_{31N} \tag{19}$$

(8) Paying careful attention to signage, sum the four voltages found in step VII to obtain V_H via:

$$V_H = V_C + V_D + V_E + V_F \tag{20}$$

Through combining Equations 14 and 15, once the value of V_H is determined, both the Hall Effect mobility and carrier concentration of the thin film sample may be acquired. Through iterative processes to minimize fluctuation of data across samples with varying resistivity values, the constant current used in this study's Hall Effect measurements was sourced at 1 μA. The electromagnet was programmed to output a magnetic field magnitude of ±5000 Gauss with its respective power source set at ± 3 A. Each voltage value gathered prior to the V_H summation (e.g. V_{24P}), seen in steps VII and VIII above, was acquired

through the real-time averaging of 1000 separate voltage measurements. The settling time, i.e. the time between separate voltage measurements during the experiment in order to allow for the dissipation of potential charge build-up within the sample, was set to 5 ms. Charge buildup across the film typically occurs only when analyzing highly-resistive samples and as the films under study are shown to be semi-conductive at their highest resistivities, the probability for charge buildup occurrence is negligible.

3.2.2 Microstructural Analysis

The first step in investigating the microstructure of amorphous thin films involves establishing which microstructural parameters may affect the thin films' performance techniques as well as the films' potential for application. In the case of *a*-IZO, multiple characteristics such as, but not limited to, surface roughness/uniformity and the microstructural phase (amorphous/semi-crystalline/crystalline) of the material are major importance. If the introduction of a ternary-dopant material causes a dramatic alteration in one of the previously mentioned properties, the potential for impactful application decreases – excluding applications which have not yet been established for use of *a*-IZO. Thus, examining the microstructural and optical effects of Al^{3+}-doping IZO is essential to provide a clear outlook on IAZO's potential future in the thin film field.

To observe the possibilities of induced film-crystallization in the IAZO films (as well as verify the amorphous nature of the baseline IZO films), *θ-2θ* X-ray diffractometry (XRD) was employed. Thin film XRD analysis, in summary, bombards a thin film with X-rays of a fixed wavelength and then utilizes Bragg's Law to identify any crystalline structures within a given material. Bragg's Law may be expressed as[82]:

$$n\lambda = 2d\sin\theta \tag{21}$$

where n is an integer signifying the order of reflection, λ is the wavelength of the applied incident X-rays (nm), d is the interplanar lattice spacing (nm), and θ is the angle of incidence (°). In Figure 3.6, a simplistic visualization of Bragg's Law may be observed, where two separate applied X-rays, ABC and A'B'C, diffract on different lattice planes (locations B and B')[83].

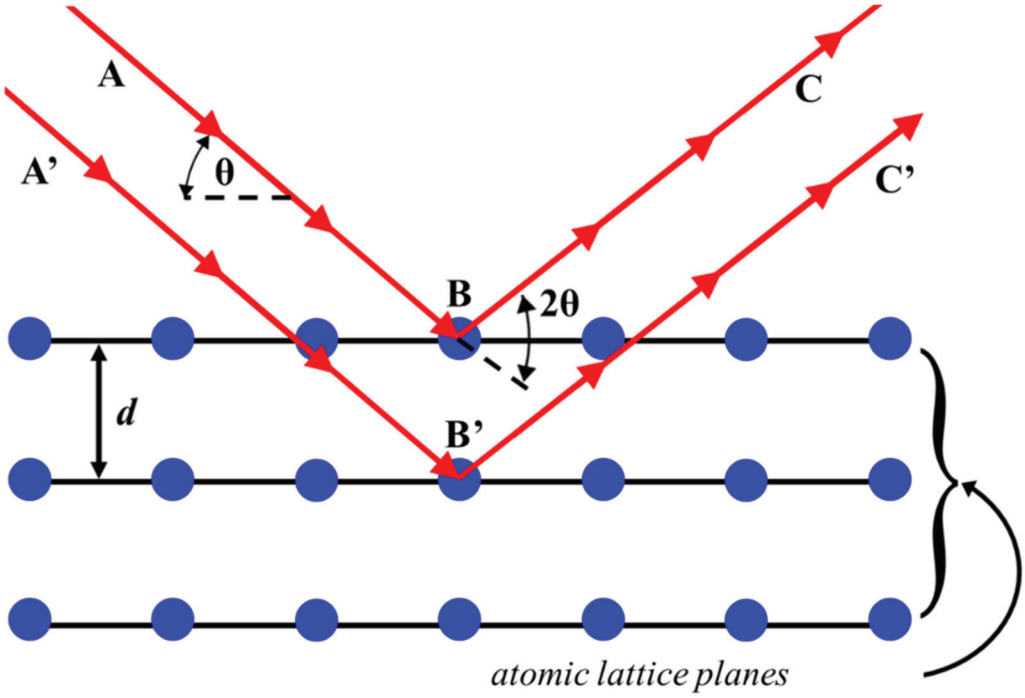

Figure 3.6. Two-dimensional visualization of X-rays projected onto a crystalline lattice via XRD. Interplanar lattice spacing is defined as *d* (nm) and the angle of incidence as θ (degrees).

When the difference in travel path length, *d*, is an integer multiple of the wavelength, XRD will produce constructive interference for that specific combination of the X-ray wavelengths, lattice planar spacing, and angle of incidence[83]. The intensity of diffraction at certain angles of incidence is acquired by the XRD system, which in turn

produces peaks of known crystalline structures in an XRD plot of incidence angle vs. diffraction intensity.

Two methods of XRD analysis may be used to identify crystalline peaks, *θ-θ* and *θ-2θ*. XRD instruments comprise of three primary tools: cathode tube which bombards the sample with x-rays, a sample stage where the material/thin film is mounted, and a detector which acquires any notable diffraction rays. To implement the *θ-θ* method, the sample stage is kept stationary while both the cathode tube and the detector move simultaneously over an established *θ* range of angles. When utilizing XRD equipment capable of *θ-2θ* analysis, both the detector and the sample stage rotate throughout the scanning process while the cathode tube remains stationary. As mentioned, this study utilizes *θ-2θ* due to the XRD equipment readily available.

To reduce noise in the resulting data, a scanning rate of 0.0021°/s over an incidence angle range of 10°-100° was decided upon, leading to a total scanning duration of ~12hr per sample. When examining pure-/doped-IZO thin films via XRD analysis (depending on how significant the wt. % of doping material is present, of course), only known In_2O_3 peaks are of priority. As the majority of IZO targets' chemical compositions currently under investigation are 10 wt. % Zn: 90% In_2O_3, the small wt. % of Zn is assumed to be negligible during the formation of crystalline peaks. The same conclusion about Zn's effect on the crystallization of *a*-IZO films can also be applied (usually) to ternary-cation doping investigations, unless the wt. % of the dopant reaches high enough values where it is deemed necessary.

3.2.3 Optical Analysis

The primary optical parameters of interest in this study are percent transmittance (%T) and optical band gap (E_G). Fortunately, E_G can be deduced from acquired %T data through the implementation of Tauc plots and thus only one optical parameter must be experimentally obtained. In this study, the employment of an ultraviolet-visible spectrophotometer (UV-vis) provided the method to obtaining the fabricated films' %T data. UV-vis spectrometers possess the ability to measure the absorbance of ultra-violet or visible light by a sample through performing a scan over a pre-established range of the light spectrum[84]. A light source within the UV-vis spectrometer provides the radiation desired, where the output is then focused into a diffraction grating – splitting the light into its component colors of different wavelengths[84]. The separate components are then projected onto the thin film sample and the wavelengths which pass through are detected, allowing one to see the films' absorbance, *A*, across the established light spectrum[84]. Light absorption values lead directly to the procurement of %T via Beer's Law[85]:

$$A = 2 - \log_{10}(\%T) \tag{21}$$

where %T is percent transmittance and A is absorbance. The %T data for all fabricated samples may be plotted against the light spectrum wavelength range desired, which in this study was set to 300 nm – 800 nm.

The implementation of additional analysis techniques, such as atomic force microscopy (AFM) and scanning electron microscopy (SEM), were desired but ultimately were not able to be performed due to the external constraints of the study. Future AFM data will give valuable insight into potential IAZO applications as it will determine whether or not Al^{3+}-doping has an effect on the surface roughness/uniformity of *a*-IZO.

Furthermore, SEM imaging would provide valuable insight to both the planar uniformity of IAZO films and the cross-sectional bonding to certain material substrates. Both of the most recently mentioned analysis techniques are discussed again in Section 5.2.

CHAPTER FOUR

Results and Discussion

4.1 Electronic Property Analysis of Al^{3+}-Doped a-IZO

Typically, when investigating the effects cation doping may have on an established amorphous oxide conducting thin film, the electrical analysis revolves around three distinct properties: carrier mobility, carrier concentration/density, and resistivity. As seen through Equation 15 in Chapter 3, all three electrical properties are related to one another, and a drastic change or shift in one will have a similar effect on another (in most cases). However, the importance of these property changes lies not necessarily within the magnitude change of the property itself, but rather in the phenomenon which is responsible for inducing the change. Unveiling how dopant materials interact with the original amorphous oxide is sometimes of more value than the comparable effectiveness of the interaction as discovering the underlying mechanisms behind the change may inspire further research more suitable for application use. Thus, using prior IZO literature to substantiate the claims made, the interacting mechanisms between Al^{3+}-dopant material and IZO thin films are described in detail later on in this chapter.

The first electrical parameter investigated during post-fabrication analysis is the film resistivity (ρ, Ω-cm). Acquiring resistivity values and trends is typically the first step in thin film electrical analysis due to the fact, seen via Eqn. 15 in Chapter 3, resistivity is a pre-requisite to determining the carrier mobility of a thin film. Furthermore, resistivity is useful as an initial indicator of whether or not a deposition was performed properly as well

as in determining if a thin film which warrants further investigation/analysis was produced. As seen in Chapter 3, Eqn. 2, resistivity is simply the sheet resistance, R_S (Ω/□), of a thin film multiplied by the thickness, t (nm). As all deposition rates were iteratively gathered for each RF power setting prior to post-fabrication analysis, all films examined were produced to be ~100nm thick – achieved by matching the deposition time (s) to fit its respective deposition rate (nm/s) and confirmed via ellipsometer measurements. Furthermore, to confirm the validity of resistivity data prior to supplementary analysis, R_S values were verified via the Keithley 4200-SCS Characterization System, seen in Figure 3.4. Three separate sets of samples for each RF power setting were fabricated at different times under the same sputter deposition parameters (excluding RF power) to ensure the reliability of the data.

As can been seen in Figure 4.1, an increase in Al^{3+} content (RF power) directly correlates to an increase in resistivity of the IAZO films, excluding RF-10W. As the resistivity values for IAZO RF-10W (~$3.8 \cdot 10^{-4}$ Ω-cm) are remarkably close to that of the baseline IZO's resistivity (~$3.1 \cdot 10^{-4}$ Ω-cm), it may be assumed that while the RF plasma beam at 10W appeared to be steady during fabrication unlike power settings <10W, it provides a negligible amount of Al^{3+}-dopant within the material. In contrast to the prior study of Al^{3+}-doped IZO via co-sputter deposition[72], a sharp decrease in resistivity was not observed across any of the sets of samples produced and resistivity values acquired from the IAZO samples fabricated at >10W instead followed the theorized trend of ideal cation dopants[15].

Concerning the increasing trend displayed in Figure 4.1, the occurrence of the positive correlation between RF power and film resistivity possesses three possible

explanations based on prior ternary-doped IZO literature [1,8,15,18,39,40,50,51,69]: (i) Al^{3+}-incorporation into IZO may work effectively as a reliable carrier suppressor in *a*-IZO films and subsequently reduces the resistivity values (ii) Al^{3+}-dopant ions may as an extra scatter site and significantly reduce the carrier mobility or (iii) both of the above. In order to identify which underlying factor is the cause of the increase in resistivity, as well as being able to compare the effectiveness of Al^{3+}-doping in comparison to other ternary-cation doping materials, both carrier concentration and carrier mobility values were obtained through the use of the Hall Effect Method described in Section 3.2.3 of this thesis.

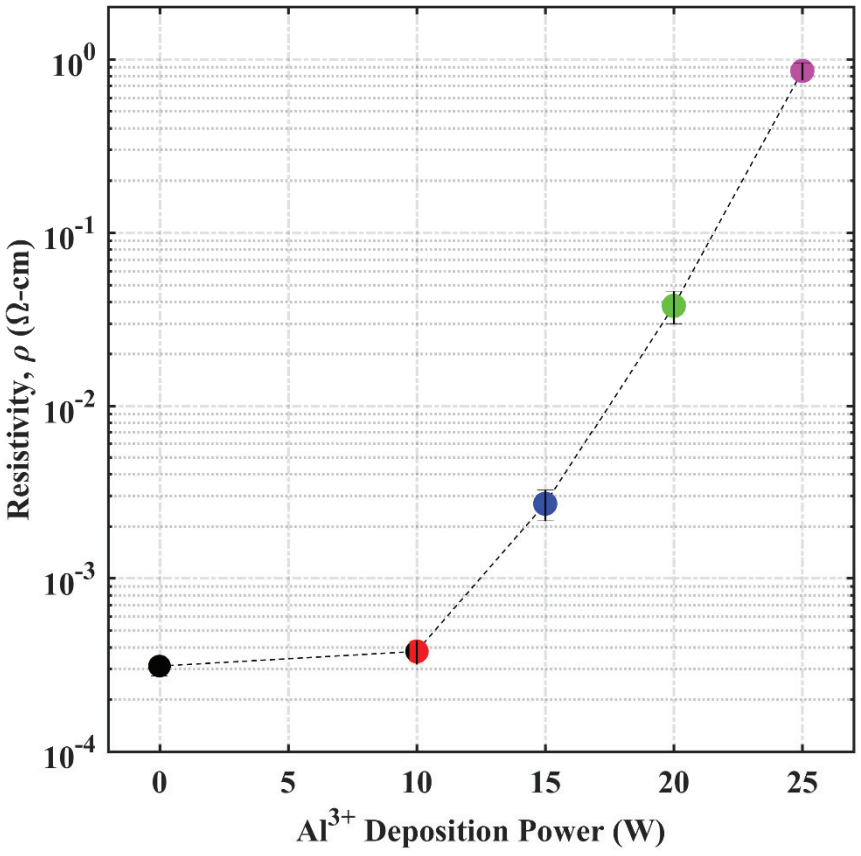

Figure 4.1. Resistivity (Ω-cm) of fabricated *a*-IZO/IAZO samples as a function of RF deposition power (W) used to deposit Al^{3+}-dopant material.

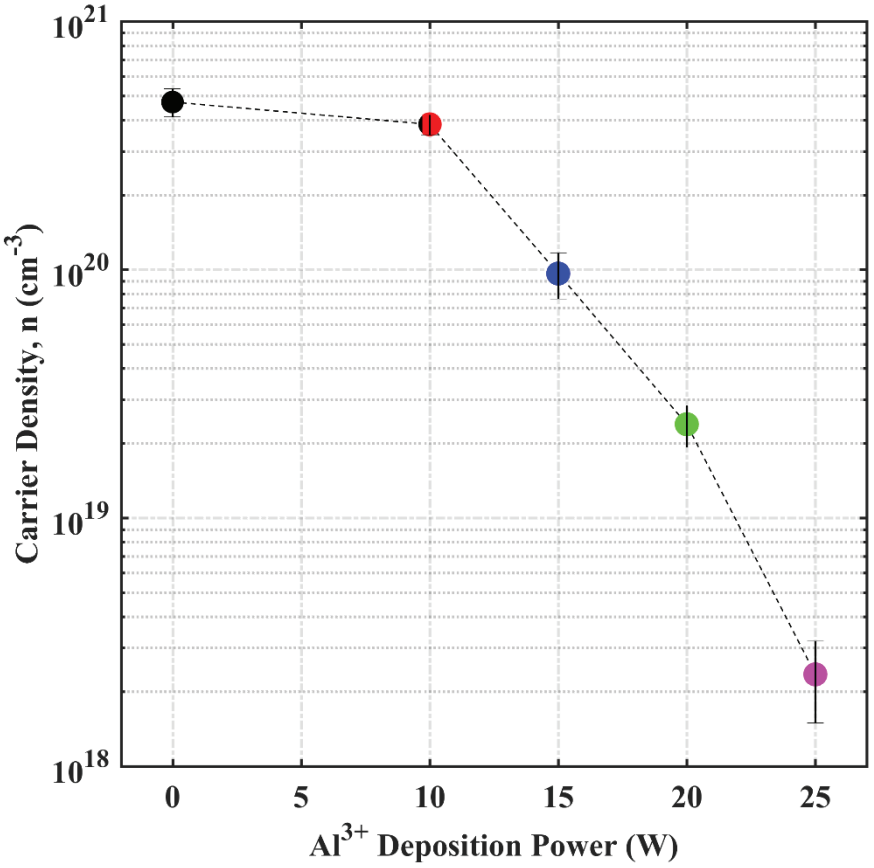

Figure 4.2. Carrier density (cm^{-3}) of fabricated *a*-IZO/IAZO samples as a function of the RF deposition power (W) of the Al^{3+}-dopant material.

As seen in Equation 15 in Section 3.2.3, n-type carrier concentration (cm^{-3}), n, is shown to be directly related to film resistivity. Figure 4.2 displays the carrier concentration of the material decreasing as a function of increasing RF power, or rather increasing Al^{3+} content in the material. The inverse trend in Figure 4.2 implies that the resistivity change seen in Figure 4.1 is due, in part, to the fact that Al^{3+} does indeed act as an effective carrier suppressor in IZO (excluding RF-10W, where, as stated prior, the changes in resistivity and carrier concentration indicate that a negligible amount of Al^{3+} is present in the film).

As theorized, using the guidelines for cation-doping established by Parthiban et al. for justification, Al^{3+}-doping data displays trends typical of other ideal ternary-cation

dopants[15]. However, at a power setting of RF-25W - which is assumed to contain the highest concentration of Al^{3+} - the carrier suppression effects only decrease the baseline IZO carrier density to a magnitude of ~10^{18} cm^{-3} from ~10^{20} cm^{-3}. As 10^{18} cm^{-3} does not meet the requirements for semiconductor application, where the desired density is <10^{17} cm^{-3}, the results indicate that Al^{3+} by itself may not be an ideal material choice for ternary-cation doping due to a carrier suppression effectiveness of only three magnitudes (~10^{3} cm^{-3}). Even though Al^{3+} should possess the intrinsic characteristics to be labeled as an ideal cation dopant for *a*-IZO[15], the limitations of carrier suppression performed via co-sputter deposition suggest otherwise.

When compared to the carrier suppression effectiveness of Ga, which reduces carrier density from a baseline *a*-IZO value of 10^{18} cm^{-3} to a doped density of <10^{13} cm^{-3}[15,18], Al^{3+} appears to lack in efficacy. Though, one must note an integral difference between this particular investigation and those which examine other ternary cation dopants is that the majority of established dopant materials have been introduced to IZO via their oxide counterpart during the fabrication process - e.g., Ga as Ga_2O_3[15,18,39,40], Si as SiO_2[34,37,42,43], and Hf as HfO_2[44-47]. The differences between metallic- and oxide-doping methods may suggest that Al^{3+}'s oxide counterpart, Al_2O_3, could prove to be more effective in carrier suppression than strictly Al^{3+}, but this claim must be further investigated before it holds any substance. An additional argument for why introducing IZO-dopants in their oxide state may be a more suitable method can through the role that oxygen vacancies possess in IZO and the interactions between the oxygen ions present in the dopant material. As it has been established that oxygen vacancies are the dominant carrier doping mechanism in IZO thin films[1,28,67], the introduction of a ternary-cation dopant in its

oxide form may suppress the generation of carriers which are formed via oxygen vacancies more effectively than that of a singular metallic dopant. Excess oxygen ions introduced to the film composition via the dopant material are likely to further suppress oxygen vacancy formation during the fabrication process then if they were absent. In addition to the possible advantages of doping via the oxide compound rather than utilizing a strictly metal target is an increased control of dopant concentration in the material. As mentioned previously, metallic targets are known to possess much higher deposition rates than that of their oxide counterpart due to their vastly superior conductivities and while Al^{3+} was deposited via RF power (which possesses a much lower deposition rate than DC power), the inability to generate steady plasma streams at <10W severely impedes the controllability of Al^{3+}-content in the film. Thus, in order to obtain truly comparable data of Al^{3+}'s carrier suppression capabilities in IZO films, a follow-up study utilizing Al_2O_3 in lieu of Al^{3+} could provide more comparable insight in terms of its effectiveness related to established IZO ternary-cation dopants – not only due to the excess oxygen ions in its chemical composition but also due to the enhanced controllability of its deposition rate.

Continuing the electrical data analysis of IAZO films, the measured carrier mobility data of *a*-IZO/IAZO films are visualized in Figure 4.3 as a function of increasing RF power (Al^{3+} content). Similar to carrier density and resistivity values observed in Figure 4.2, RF-10W's carrier mobility (~43.4 cm^2/Vs) exhibits little variation from that of the baseline *a*-IZO measurements (~42.9 cm^2/Vs), proving further that, under the current sputter deposition conditions, an RF power setting of 10W provides a negligible amount of doping content within the resulting film. As RF power increases, IAZO carrier mobility follows a

steep declining trend, falling to ~24.9 cm^2/Vs at 15W and further plummeting to <10 cm^2/Vs at 20W (~7.5 cm^2/Vs) and 25W (~3.4 cm^2/Vs).

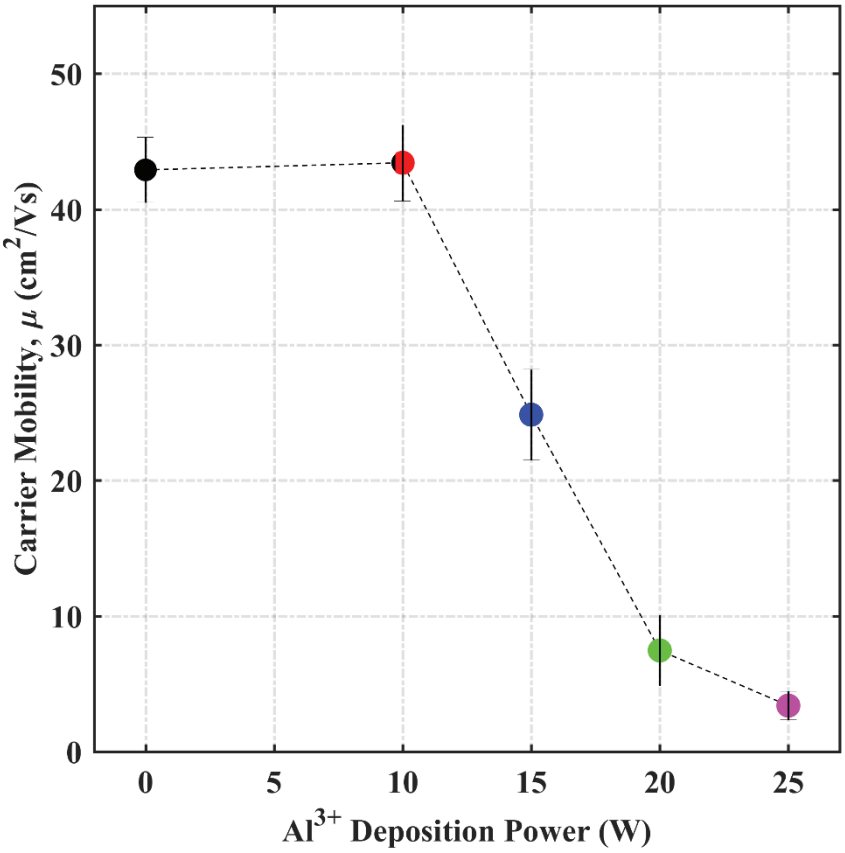

Figure 4.3. Room temperature carrier mobility (cm^2/Vs) of IZO/IAZO samples as a function of Al^{3+} deposition power (W).

15W-IAZO, while possessing a carrier mobility (~24.9 cm^2/Vs) almost less than half then that of baseline *a*-IZO, still maintains a respectable mobility in comparison to conventionally used *a*-Si:H (<1 cm^2/Vs)[1,8,9,15,18,22,33]. However, the carrier density observed at 15W (~10^{20} cm^{-3}) is still three magnitudes higher than the maximum concentration limit of semiconductor applications (10^{17} cm^{-3}). Overall, the mechanism presumed responsible for the sharp decline in carrier mobility in respect to an increase in Al^{3+}-doping content is most likely explained through the common effect of ternary-dopants

acting as additional scattering mechanisms in *a*-IZO[1,15,50,51] and subsequently reducing carrier transport effectiveness. While the resistivities and carrier concentrations of IAZO films are reported in the 2010 investigation[72], the carrier mobilities are not, so direct comparison of the effects of Al^{3+}-doping on the carrier mobility of IZO is unattainable. Furthermore, as the resistivity and carrier concentration trends presented in the 2010 study[72] and those displayed by this study do not support one another, it is reasonable to state that a carrier mobility comparison would not provide any quality insight.

In Figure 4.4, the carrier mobilities (cm^2/Vs) of the IZO/IAZO samples are depicted a function of carrier concentration (cm^{-3}). The trend in Figure 4.4 follows typical trends in IZO literature, where carrier mobility is observed to increase with an increase in carrier density until the concentration, for lack of a better term, reaches a critical value where mobility either decreases or displays no visible change[1,28]. This common phenomenon is explained through the competition of two separate carrier transport mechanisms, charge-screening and the formation of excess scatter sites[1,15,27,28,50,51].

The effect of charge screening is observed to occur when excess carriers in a thin film effectively work to prevent scatter sites from negatively affecting the transport of mobile carriers. In laymen's terms, one can visualize charge screening with an analogy to a "screen" in basketball – where the additional charge carriers act as the third party, preventing the defender (scatter sites) from pursuing (affecting) the ball-carrier (charge carriers). This charge-screening effect is observed to dominate the carrier transport mechanisms in IAZO films up until carrier density values of $\sim 10^{20}$ cm^{-3}, seen in Figure 4.5, where the excess charge carriers at values greater than the threshold begin to act as additional scattering sites, preventing efficient carrier transport throughout the material.

Ultimately, this threshold point proves to be consistent with prior IZO literature, as IZO's critical value typically occurs around ~10^{20} cm^{-3}-10^{21} cm^{-3}. Thus, it can be stated that in this study, Al^{3+}-doping does not significantly affect the point at which dominating *a*-IZO carrier transport mechanisms shift.

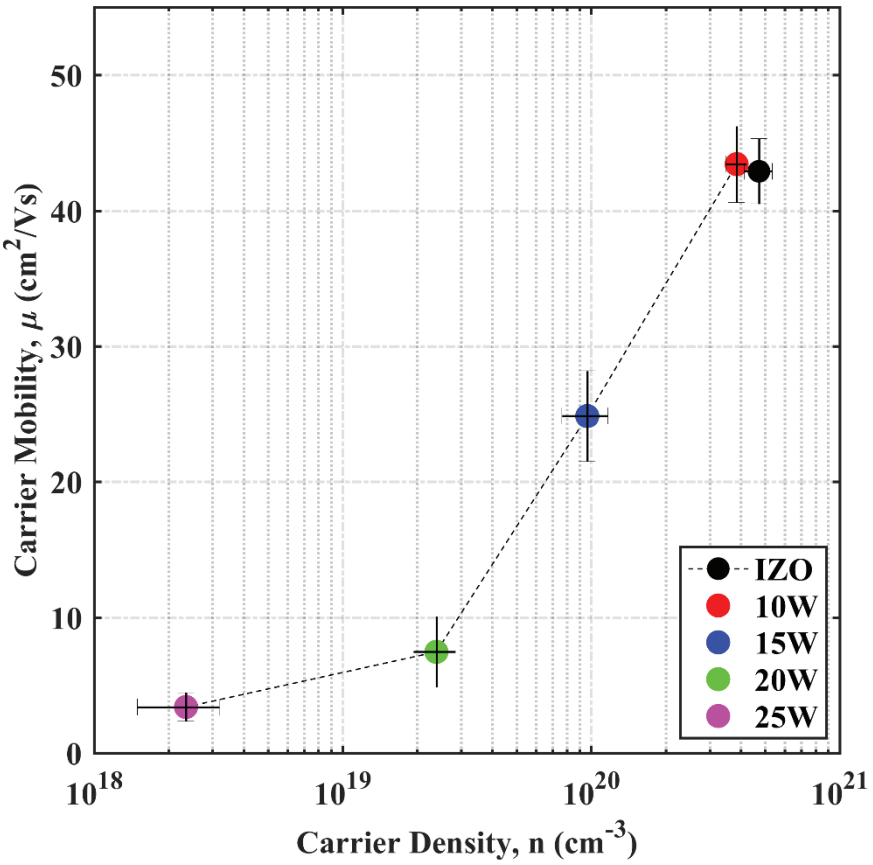

Figure 4.4. Room-temperature carrier mobility (cm^2/V-s) of fabricated *a*-IZO/IAZO samples as a function of carrier density (cm^{-3}).

4.2 Microstructural and Optical Effects of Al^{3+}-Doping a-IZO

Investigating the optical and microstructural effects of introducing a ternary-cation dopant to IZO is crucial in determining its application potential as well as in providing insight for future research. In this study, the specific optical parameters investigated are the effects Al^{3+}-doping has on the %T and the E_G (eV) of IZO films. Microstructural data

gathered includes XRD measurements of both as-deposited and air-annealed IZO/IAZO, as well as preliminary AFM images providing film-surface visualizations (not completed due to limited AFM access).

4.2.1 Al^{3+}-Doping Concentration Effects on Optical Properties

As can be observed in Figure 4.5, an increase of RF deposition power, and subsequently an increase of Al^{3+}-dopant, leads to a significant decrease in the overall %T of IZO/IAZO films. As expected, a power setting of RF-10W appears to have no impact on the optical transmittance (%T) of IZO films. In general, it can be observed that an increase in RF power (>10W) leads to an overall decrease in %T across all samples. A decline in %T with increasing Al^{3+} content is to be expected, a Al^{3+}'s classification as a metal specifies an overlapping band gap which directly relates to a decrease in optical transparency[86]. While RF power settings of 10W and 15W possess reasonable visible regime transparencies in their as-deposited state (88.96% and 82.67% at λ = 550 nm, respectively), 20W and 25W exhibit large drops in %T (64.88% and 46.73% at λ = 550 nm, respectively), leaving their values short of the preferred %T of >80%[2,3,8-12,17,22,23] for amorphous oxide applications in transparent devices. The clear blue-shift in response to increasing RF power can be seen via the Tauc plots shown in Figure 4.6, where the square of absorption coefficients, α, are shown as a function of photon energy. The trend observed in Figure 4.6 provides further evidence of Al^{3+}-doping's adverse effect on the optical transparency of IZO. As it is established that IZO acts a direct semiconducting material [26,87], extrapolation of the linear regimes of α^2 vs. hv provides the optical band gap for each IZO/IAZO film analyzed.

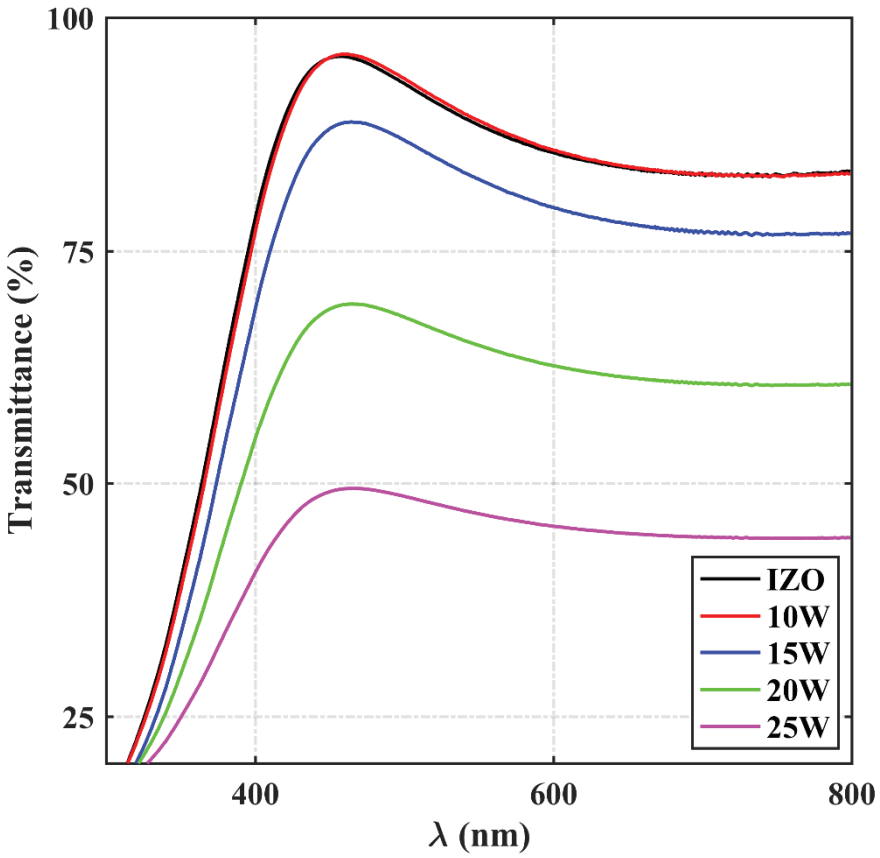

Figure. 4.5. %T of the IZO/IAZO films as a function of wavelength (nm) across the visible spectrum (~300nm–800nm).

In Figure 4.6, E_G values are plotted as a function of RF power, displaying an overall negative change in bandgap of ΔE_G = ~0.4 eV from baseline IZO to RF 25W-IAZO. The underlying reasoning for a decrease in bandgap as RF power increases is directly related to the carrier density trend observed in Figure 4.2. Through the phenomenon known as the Burstein-Moss (BM) effect, the shifting of the absorption edge to a reduced wavelength seen in Figures 4.5 and 4.6 is due to the increased suppression of electrons (carriers) within the conduction band of IAZO films as RF power increases [41,88-90].

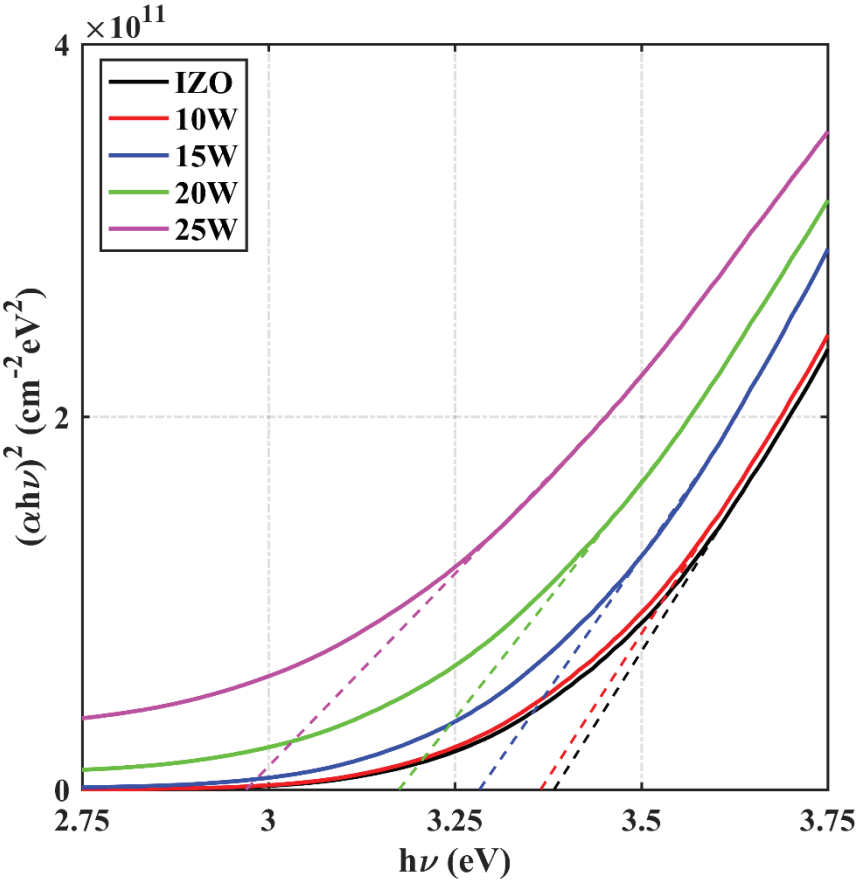

Figure 4.6. Tauc plots of IZO/IAZO films.

The relationship between E_G and carrier density, seen in Figure 4.7, can be shown through the BM equation [41,91]:

$$\Delta E_G = \left(\frac{h^2}{8m^*}\right)\left(\frac{3n}{\pi}\right)^{2/3} \tag{21}$$

where n is carrier density (cm^{-3}), m* is the reduced effective mass of the electron (kg), h is Planck's constant, and ΔE_G is the change in optical gap (eV). To further verify the claim of a BM-shift occurrence, as well as visualize the relationship between the two variables, optical band gap is linearly plotted against logarithmic carrier density in Fig, 4.8. This

semi-log linear relationship is consistent with prior IZO literature, where IZO is shown to decrease in optical band gap as carrier concentration is reduced [9,29,41,92].

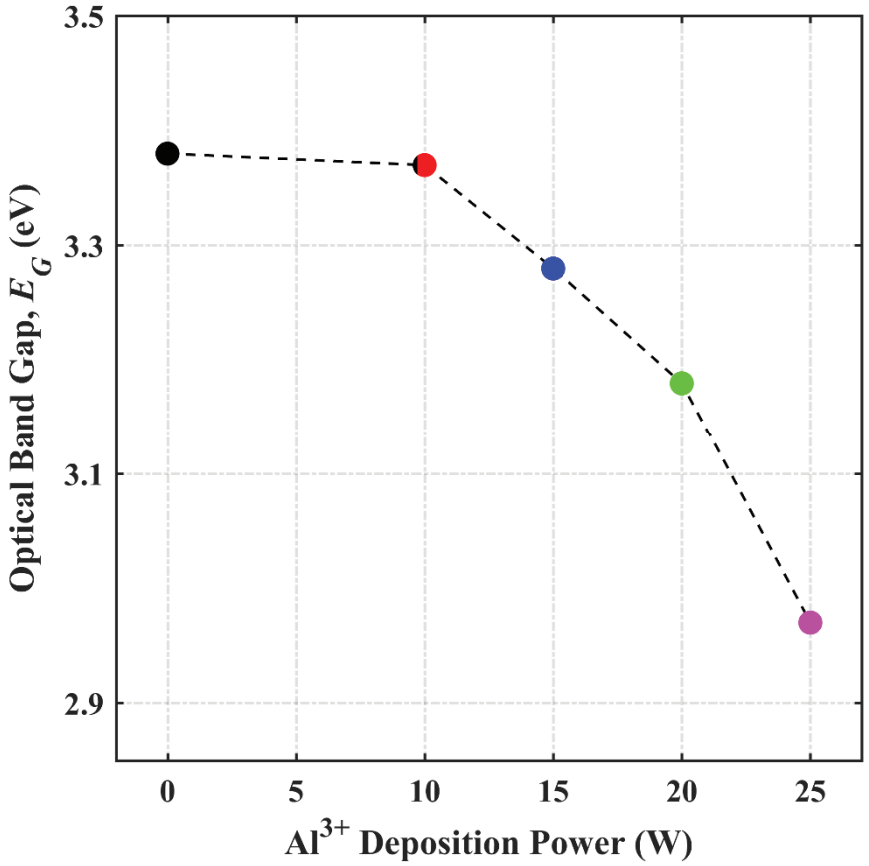

Figure 4.7. Optical bandgap, E_G (eV), of the IZO/IAZO films as a function of increasing Al^{3+} deposition power (W).

4.2.2 Al^{3+}-Doping Concentration Effects on Microstructural Properties of a-IZO

In Figure 4.9, XRD data of as-deposited IZO/IAZO samples across a *θ-2θ* scan range of 10°-100° is displayed. In direct contrast to the 2010 IAZO study[72], the introduction of an increasing amount of ternary Al^{3+}-dopant is shown to have no effect on the amorphous-phase composition of IZO films. Previously, Sun et al. reported that IAZO films fabricated at RF powers of 9W, 11W, and 16W all possessed crystalline peaks at ~33°, where the authors attributed the occurrence of peaks to the formation of either α-

A_2O_3 (32.778°), β-Al_2O_3 (32.902°), γ-Al2O3 (32.778°), or unnamed Al_2O_3-paramorphs (33.026°,33.407°) [72].

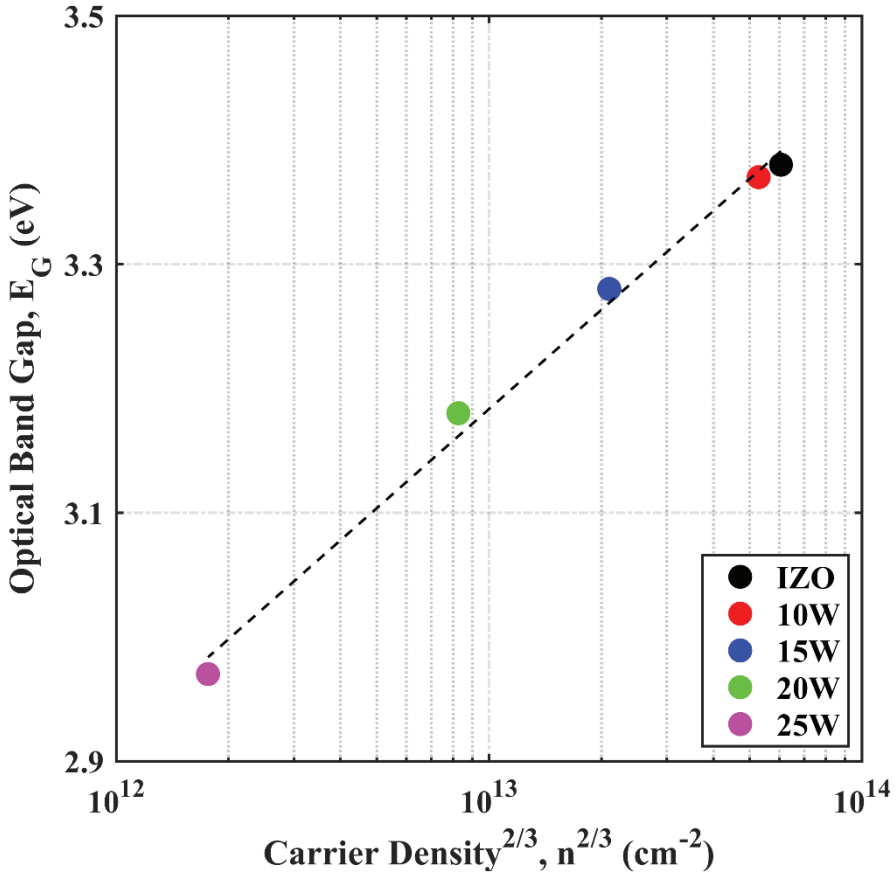

Figure 4.8. Optical bandgap, E_G (eV), of IZO/IAZO films as a function of (carrier density)$^{2/3}$ (cm^{-2}).

While the study's explanation for the occurrence of these peaks is reasonable (stating that the Al dopant ions reach critical nucleus size at higher RF powers, i.e. higher amounts of Al content[72]), the lack of sample thickness consistency across depositions combined with the inconsistency in electrical property data brings suspicion to the reliability of the claims[72]. Furthermore, as the IZO targets used in both studies are comprised of 90 wt.% In_2O_3 and 10 wt. % Zn, the probability that small amounts of Al^{3+} dopant material would

promote Al_2O_3 crystallite formation at room-temperature is suspect. More importantly, however, is the fact that Al_2O_3 is shown in other studies to only take the form of *a*- or γ-Al_2O_3 microstructures when deposited via sputter deposition[93,94], compounding the extremely low probability of α-/β-/unnamed paramorph-Al_2O_3 nanocrystallite formation. In the current study, no variations of Al_2O_3 crystalline peaks were visible in the entirety of the XRD analysis of as-deposited and annealed films. As the potential benefits of utilizing amorphous films in lieu of semi-crystalline/crystalline films are substantial, such as flexible device compatibility and higher surface uniformity, the validity of whether or not Al^{3+}-doping plays a role in the crystallization of as-deposited *a*-IZO films warrants further investigation.

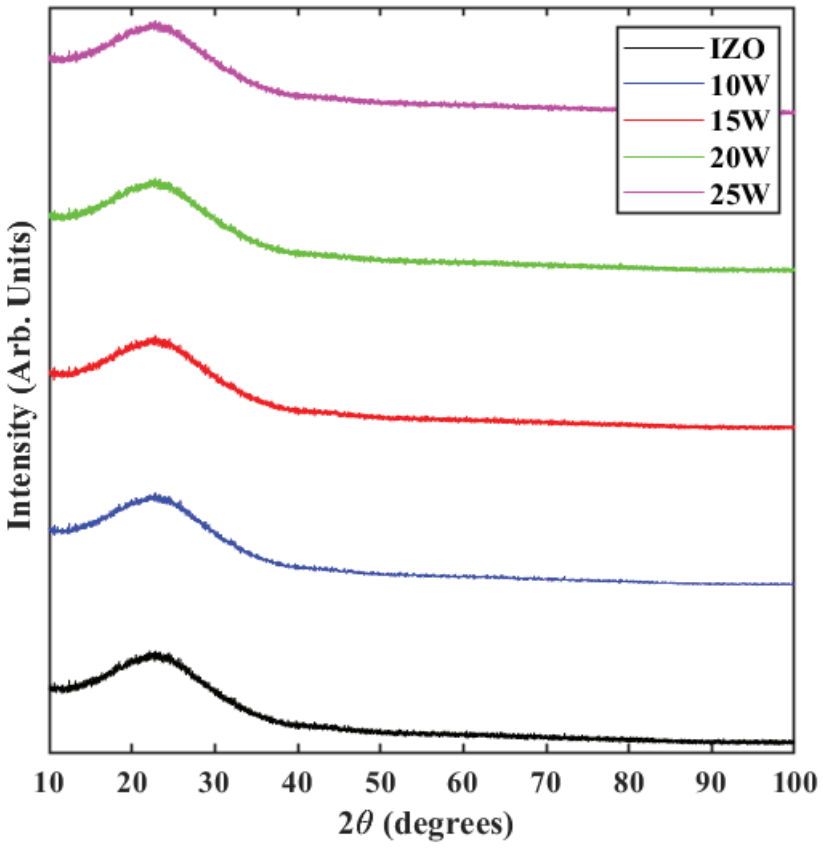

Figure 4.9. XRD analysis of as-deposited IZO/IAZO thin films across a scanning range of $10^o < 2\theta < 100^o$.

To obtain more information about the microstructural effects of Al^{3+}-doping IZO, additional XRD analysis was performed on both IZO and IAZO films subject to post-fabrication heat treatment. Samples were air-annealed at 500ºC for ~1hr, as previous IZO literature has found that *a*-IZO's onset-of-crystallization occurs ~500ºC[1,9,10,28,38]. In Figure 4.10, air-annealed IZO/IAZO XRD data reveals that increased Al^{3+} content in *a*-IZO films effectively delays the onset-of-crystallization in IZO at RF powers >10W. The annealed-IZO sample is consistent with previous IZO annealing studies, corresponding to In_2O_3 crystalline planes at 21.62º ⟨211⟩, 30.68º ⟨222⟩, 35.54º ⟨400⟩, 42.14º ⟨332⟩, 45.82º ⟨431⟩, 51.59º ⟨440⟩, and 60.49º ⟨622⟩. Consistent with the electrical and optical data collected, samples doped at an RF power setting of 10W contained negligible amounts of dopant material and thus undergo crystallization under the same conditions as the baseline *a*-IZO samples. However, at samples doped at powers >10W, the amorphous-to-crystalline transitions which IZO and 10W-IAZO undergo are either significantly reduced or absent entirely. The slight shoulder peak observed for 15W-IAZO in Figure 4.10, located at ~30º-34º, indicates the film may be semi-crystalline as it lines up with the appearance of In_2O_3's preferred orientation of ⟨222⟩. However, this claim cannot be confirmed without reliable AFM or SEM imaging data (which, as stated earlier, was not able to be obtained during this study). IAZO films fabricated at 20W and 25W, however, appear to be completely amorphous after being subjected to 1hr air-anneals at 500ºC, indicating that Al^{3+} may act as a viable ternary-cation dopant to be used in enhancing the amorphous-phase thermal stability of IZO thin films.

While some AFM/SEM images were obtained during the duration of this study, time limitations and external factors limited the ability to gather wholistic data sets which would

have provided further comparable and meaningful analysis to the study. It is strongly suggested that AFM/SEM images are obtained in the future to investigate more of the microstructural effects Al^{3+}-doping may have on IZO thin films.

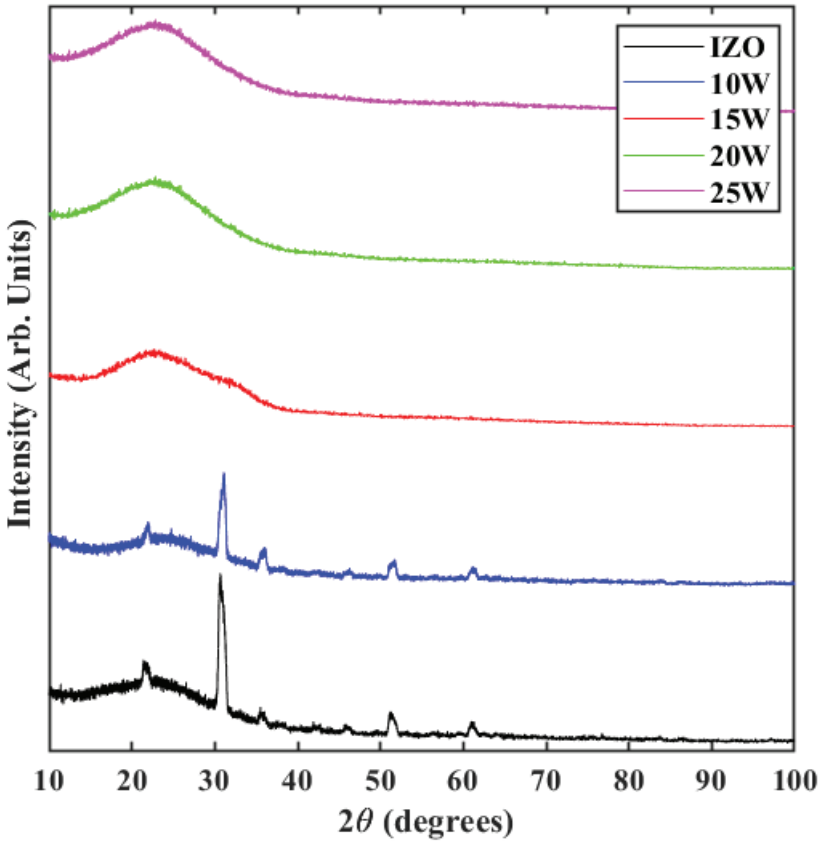

Figure 4.10. XRD analysis of annealed IZO/IAZO thin films across a scanning range of $10^{o} < 2\theta < 100^{o}$.

CHAPTER FIVE

Conclusions, Future Work, and Contributions

5.1 Conclusions

In conclusion, this study has demonstrated that the utilization of Al^{3+} as a ternary-dopant material in *a*-IZO films via UHV co-sputter deposition exhibits significant potential for enhancing amorphous-phase thermal stabilization in IZO as well as working as an effective carrier suppressor. Through an iterative process, optimal sputter parameters for each *a*-IZO/IAZO film were determined such as deposition power (DC/RF), working/base pressures, substrate rotation speed, T-s distance, required pre-sputter time, and duration of deposition. Films' electrical properties, such as resistivity, carrier mobility, and carrier density, were gathered via the implementation of a custom-built four-point probe and an integrated Hall Effect high-field electromagnet system. Microstructural analyses consisted of θ-2θ XRD scans of both as-deposited and air-annealed (500ºC) films. Optical parameters, such as %T and optical band gap were collected via UV-vis spectroscopy.

Foremost, the introduction of Al^{3+} as a ternary-cation dopant has been shown to increase the thermal stability of IZO's amorphous-phase, delaying the onset-of-crystallization to air-annealing temperatures >500ºC at RF powers of 20W and 25W. As *a*-IZO crystallizes at ~500ºC[1,9,10,28,38], confirmed via the XRD data of the baseline IZO sample in Figure 4.10, further study will allow for the realization of Al^{3+}'s full potential as a thermally-enhancing ternary-dopant in IZO.

Additionally, the insertion of Al^{3+} into the IZO matrix during film fabrication is shown to effectively suppress carrier generation via oxygen vacancy formation. At RF power levels of 15W, 20W, and 25W, carrier densities are suppressed from as-deposited *a*-IZO's density of ~$4.5 \cdot 10^{20}$ cm^2/Vs to ~$9.6 \cdot 10^{19}$ cm^2/Vs, ~$2.4 \cdot 10^{19}$ cm^2/Vs, and ~$2.3 \cdot 10^{18}$ cm^2/Vs, respectively. As stated before, RF-10W films are presumed to possess negligible amounts of dopant in the material and are considered to be pure-IZO. The effects Al^{3+}-doping had on IZO's overall carrier concentration lined up with the change in optical band gap, explained via the Burstein-Moss Effect[41,88-90] in Chapter 4. However, optical analysis of the IAZO films also suggests that the use of a metallic Al^{3+} target during co-sputter deposition may not be the optimal method of introducing Al^{3+} to the IZO system, as transmittance values drastically declined with increasing amounts of Al^{3+} content – hampering its potential for transparent thin film application. When examining this study in retrospect, considering both the lack of effectiveness in carrier suppression and adverse transmittance effects, one must consider that the metallic-oxide material of Al_2O_3 may yield more promising results than the strictly metallic Al^{3+} target used. Furthermore, Al_2O_3 is a known insulating material (i.e. wide band gap)[95-97] and has been shown to effectively widen the band gaps of certain metallic-compound thin films[98,99], indicating that Al_2O_3-doping may actually increase the overall %T of IAZO films.

Unfortunately, when comparing the results of this analysis to the IAZO study performed in 2010 for further insight and verification of trends, one may not be able to determine the validity of which claims ring true[72]. However, in accordance with Parthiban et al.[15], the results in this study suggest that Al^{3+}-doping behaves as one would

expect an ideal ternary doping cation to prior to experimentation. Thus, it remains that Al^{3+}-doping shows potential for use as a carrier suppressor in IZO.

5.2 Future Work

The unfinished work necessary to prepare this study for publication primarily consists of AFM/SEM imaging, EDX analysis of thicker films, and a re-visiting of sample fabrication/analysis due to the time that has transpired since the findings. AFM/SEM imaging would not only provide useful visualization of the films' nanostructures, but also give valuable insight to the effects of Al^{3+}-doping on *a*-IZO's low surface roughness. As surface roughness is a key characteristic when determining if a thin film material is suitable for multilayer-device application, IAZO AFM images would shed light on its potential in TFT channel-layer application. Furthermore, utilizing EDX to establish the chemical compositions of fabricated IAZO films and the subsequent weight percentages (wt. %) of Al:In:Zn:O within each film would provide clarity to the effects of Al^{3+}-doping *a*-IZO, as well as help in determining the effects of heightening RF power on Al^{3+}'s wt. %. EDX analysis would also provide the researchers by providing comparable chemical compositions to that of the 2010 study performed by Sun et al.[72]. To help understand the mechanisms behind the thermal stability enhancing effects of Al^{3+}-inclusion in IZO, temperature-applied resistivity vs. time measurements could be performed. By annealing one set of fabricated samples (e.g. RF-20W) for ~24hr at incrementally-increasing annealing temperatures and recording resistivity measurements over that period, the effects of Al^{3+}-doping on the activation energy of *a*-IZO could be established, providing more insight into the thermally enhancing effects. As prior data implies that Al^{3+}-doping

enhances the thermal stability of IZO, it is assumed that the thermal-induced activation energy required to alter IZO films would also be enhanced through Al^{3+}-doping.

To fully realize the potential of aluminum-inclusion in IZO, one must consider that the oxide compound of Al^{3+}, commonly known as alumina (Al_2O_3), may yield better results than doping via pure-Al^{3+} target material. Sun et al. performed another study of Al^{3+}-doped IZO where, in fact, Al^{3+} was introduced as Al_2O_3[30], yet the newer study is presented in an identical manner to the 2010 study[72] and thus is believed by the researchers in this present study to not be completely accurate. In Chapter 2, it is presented that the dominant carrier generating mechanism in IZO is oxygen vacancy formation, indicating a further suppression of oxygen vacancies would prove to be more effective. Thus, while an observable decrease in carrier concentration (~10^3 cm^{-3} at RF-25W) still takes place due to an increase in Al^{3+}-doping material (seen in Chapter 4), Al_2O_3 may prove to be a more effective carrier suppressor, i.e. oxygen vacancy suppressor, due to the oxygen ions available in its chemical structure. Furthermore, as mentioned in Section 5.1, Al_2O_3's wide band gap[95-97] may actually benefit the optical properties of IAZO films, potentially widening the band gap of IAZO and increasing overall %T. To further argue the method of ternary-cation doping via their oxide-compound counterparts, the majority of previous ternary-doped IZO studies have involved oxide states of the dopant material[15,18,34,37,39,40,42-47] and a subsequent investigation into the effects of Al_2O_3-doping IZO would provide more reliable and comparable results.

5.3 Contributions

Over the course of the time taken to complete a master's degree, the author of this work contributed to both the advancement and completion of numerous academic projects

in addition to the one detailed in this thesis. While this section will not go into full detail of each project the researcher helped with, it will summarize the works which required substantial effort and time.

5.3.1 To Written and Published Works

The Effect of O_2 Fraction in the Sputter Gas on the Electrical Properties of Amorphous In-Zn-O and the Thin Film Transistor Performance[1]. The master candidate's first contribution to a published paper as well as an introduction to the academic community, where the individual gained experience in the realm of journal paper writing and publication process – gaining the opportunity to contribute towards the completion of the publication. This paper involved investigating varying the O_2 content in the sputter gas during the fabrication of IZO thin film layers and the impact it had on the electrical, optical, and microstructual properties of the material.

Oxidative Chemical Vapor Deposition: Nanostructured Unsubstituted Polythiophene Films Deposited Using Oxidative Chemical Vapor Deposition: Hopping Conduction and Thermal Stability (Adv. Mater. Interfaces 9/2018)[19]. This study provided the master's candidate with the opportunity to contribute towards the completion of the publication in three separate facet: (i) authoring contributions particularly with the abstract and figure analyses, (ii) figure modeling through the utilization of 3-D Computer Aided Drawing (CAD) to depict an enhanced visualization of polythiophene nanostructural SEM images, and (iii) the opportunity to personally design the Frontispiece of the journal as seen in Figure 5.1 (once again utilizing CAD software).

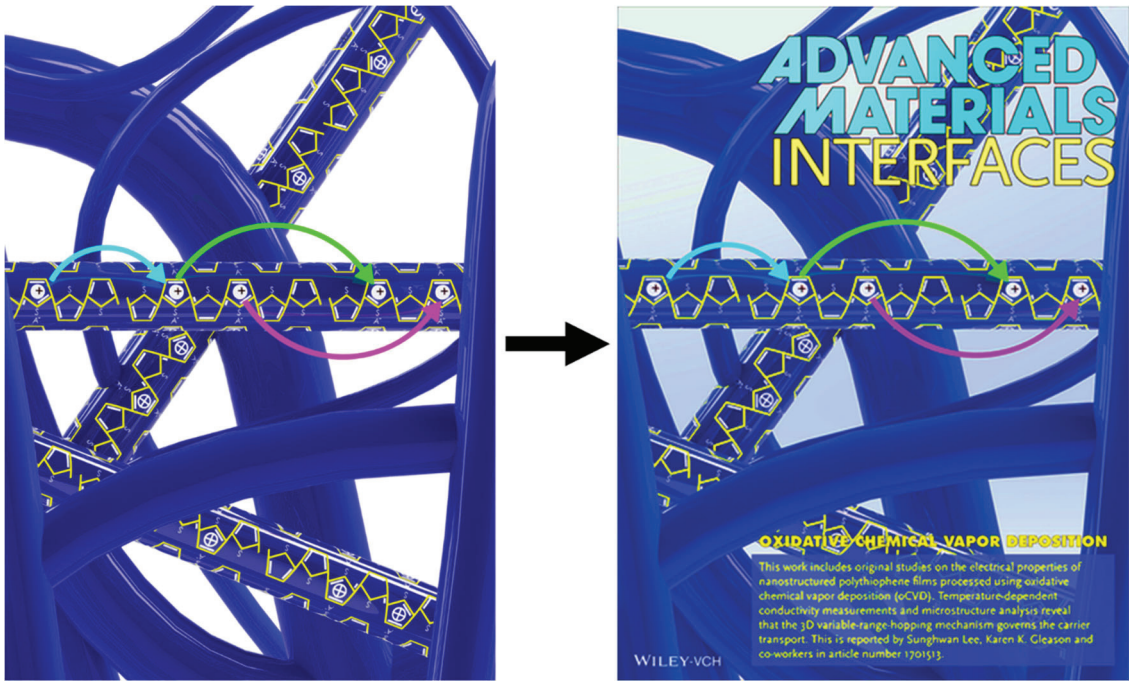

Figure 5.1. Author-designed CAD diagram (left) selected as the Frontispiece cover photo (right) for Wiley's Advanced Materials Interfaces: Volume 5, Issue 9[19]. Right photo taken from Wiley's online database[20].

AZO investigations and writings. A collaborative effort involving a faculty advisor, three separate master's students, and one undergraduate student. The faculty advisor initiated and led the collective project via the procurement of experimental data at Harvard University, where the author of this thesis then led the other group members through an in-depth analysis of the study's findings with the end-goal of high-impact publication. Due to external reasons, this completed study has not yet been put forward for review - even though the paper as finalized and deemed ready for submission - and thus the topics/results of the study cannot be further discussed.

5.3.2 To On-Going Studies and Investigations

SnO_2 iterative depositions and studies. An experimental investigation into SnO_2 thin films and their potential for use in p-n junction applications. The individual worked through months of iterative sputter depositions - changing each variable in the sputter machine in order to establish SnO_2 trends based on fabrication parameters. Ultimately, external and uncontrollable factors pushed this project to the side and it was taken over by an undergraduate, mentored by the master's candidate.

Interfacial contact properties of transition-metal oxide electrodes (3) and PEDOT Channel Layers. A straightforward study investigating the interfacial contact properties between three TCO materials with the organic thin film, PEDOT. TCO electrode parameters were iteratively optimized by the student, along with the assembly and encoding of analysis instruments. Interfacial properties were to be collected through employing technique known as the Transmission-Line-Method (TLM), which can be seen in Figure 5.2. Eventually, the obstacle of utilizing a newer sputter deposition machine interfered with the ability to deposit distinct electrode layers sputter deposition machine interfered with the ability to deposit proper electrode films.

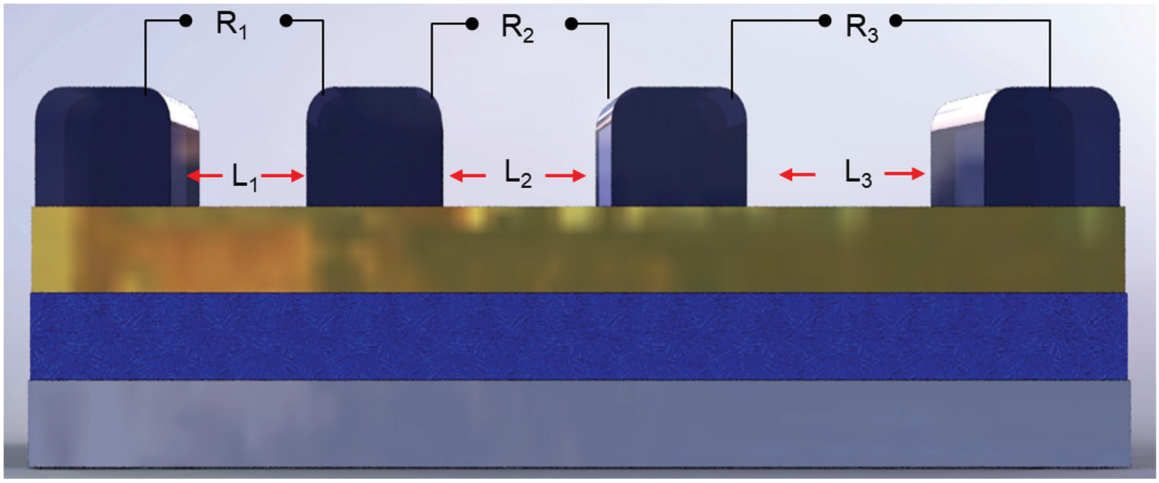

Figure 5.2. CAD model of a TLM-patterned TFT. The TLM method shown in this figure utilizes four increasingly-spaced (i.e. $R_1 < R_2 < R_3$) electrode layers (four protruding formations on top of film) to extract the interfacial contact resistance, R_C, between the electrode and channel (uppermost rectangular layer) materials. By plotting the resistances (R_1, R_2, R_3) as a function of electrode separation (L_1, L_2, L_3), the y-intercept may be extrapolated which in turn is equal to $2 \times R_C$.

APPENDIX

Standard Operating Procedures for JEOL SEM
Baylor Research and Innovation Collaborative

2016

JEOL SEM Standard Operating Procedures

Before-operation Procedures:

i. Just outside of the SEM room's door, check the chiller's water level.
   a. Unscrew yellow cap and lift up, if water level is:
      i. Above the white probe, return cap and move to next step.
      ii. Below the white probe, return cap and contact the front desk in order to obtain distilled water.

ii. Behind the SEM, check the two pumps' oil levels.
   a. If oil level is:
      i. Not within the red circle, refill or contact a regular SEM user for help with maintenance.
      ii. Within the red circle, move to next step.

Operating Procedures:

iii. On the desktop, open the program SEM Main Menu.

iv. On the lower left hand side of the opened window, ensure that the large EVAC and High Vacuum buttons are highlighted.
   a. This is the stand-by state of the SEM.

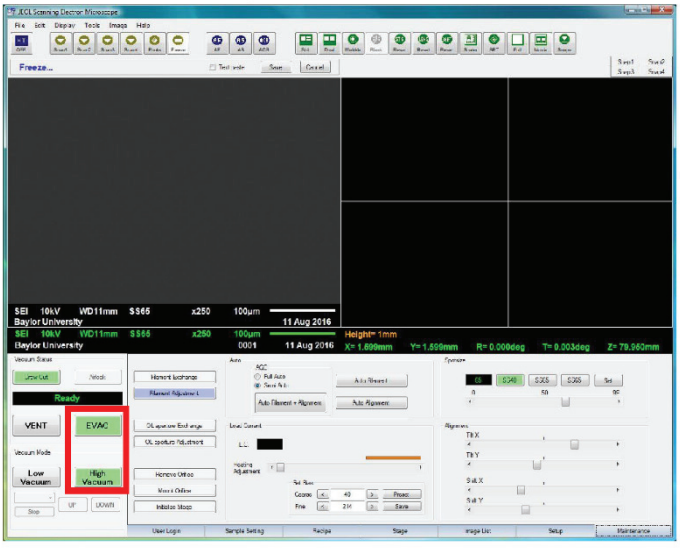

1

v. On the bottom of the window, select User Login, click your name and select Log On.

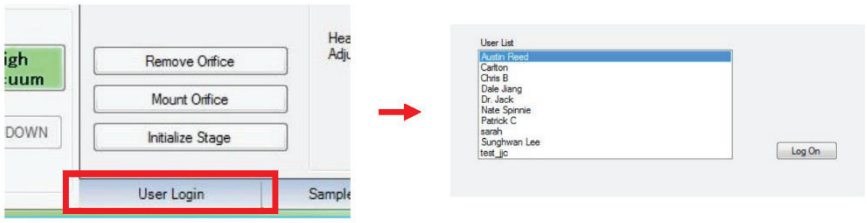

vi. Next to the User Login tab, select the Sample Setting tab.

a. In order to load the sample, select Vent.

i. Wait until blinking stops to open door.

ii. Carefully load the sample and SLOWLY shut the door.

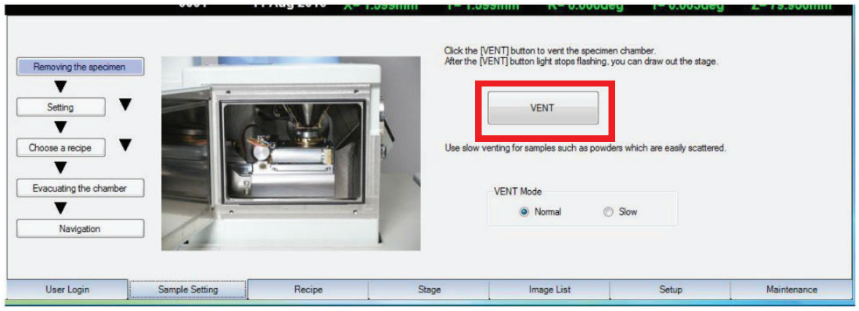

b. Follow the arrows down to Setting.

i. Where the box has an input height in millimeters, enter the specimen's protruding height above the holder box (this ensures that the lens will not contact the specimen).

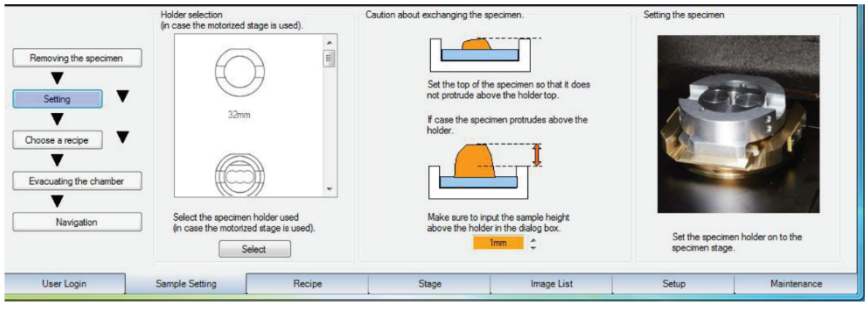

2

c. Go to Choose a recipe.
    i. Select the category that the specimen falls under and select the sample conditions.

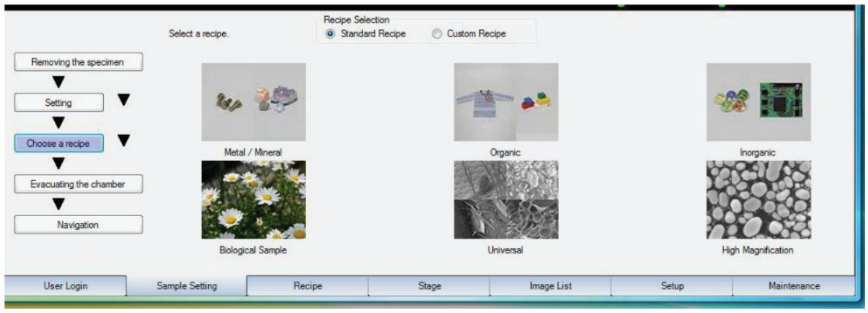

d. Next, move to Evacuating the chamber and select either High Vacuum Mode or Low Vacuum Mode.
    i. Once vacuum mode is selected, click EVAC.
        1. Wait until blinking stops.

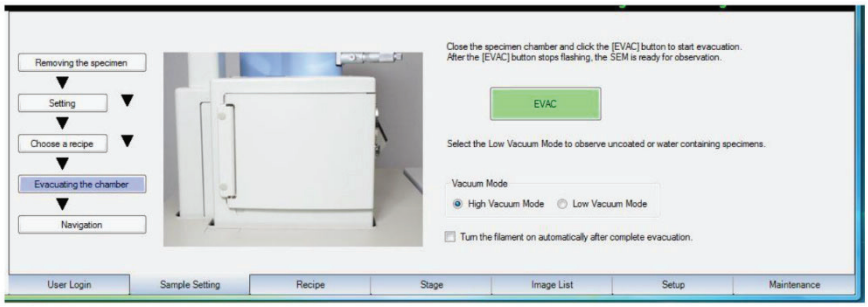

vii. Move to the Stage Tab.
    a. Ensure that the Z height, on the furthest right of the screen in green, is at 80.000 mm.
        i. If not, double-click Z and type 80 and select Move.
    b. On the left, select SNS Capture.
        i. Wait until the image acquisition stops running.
        ii. On the bottom picture with the cross, select the location on the specimen to be observed.

1. Wait until the stage stops moving.

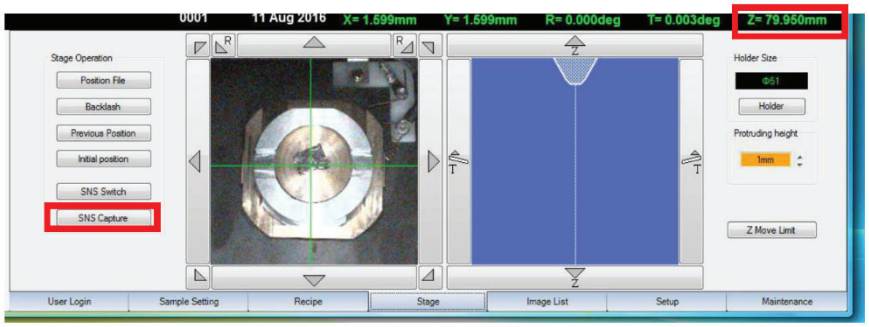

viii. Go to the Maintenance tab.
   a. In the middle lower-section of the page, slide the heating adjustment to where the right edge of the box touches the left edge of the orange rectangle.

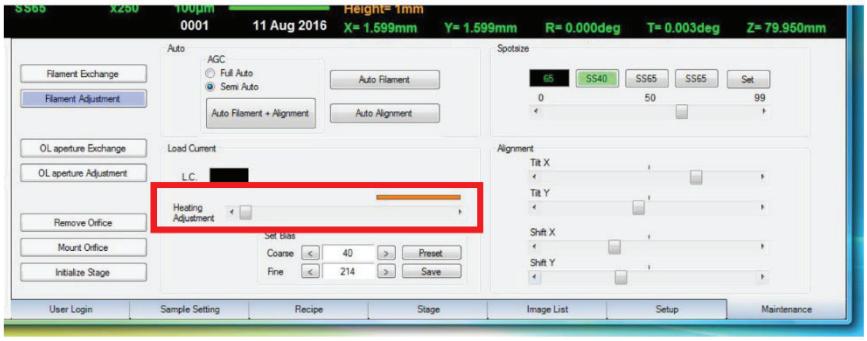

ix. On the upper left-hand corner of the page, click the HT button.
x. Double click the voltage setting and select which voltage to use for the sample.
   a. The image should appear.

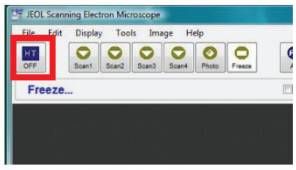

4

xi. Use the control panel to acquire the image desired.
xii. In order to save a picture:
   a. First, select Scan 3 in order to determine if picture quality is acceptable.
   b. Then, select Freeze, check the Text Paste box and select Save.

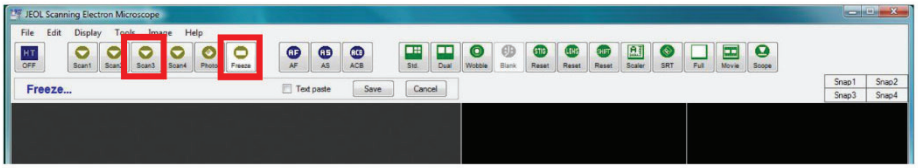

Shut-down Procedures:

xiii. First, turn off HT.
xiv. On the Maintenance tab, slide the heating adjustment back to off state.
xv. Reset the Z height to 80.00 mm, and then go to the Stage tab and select Initial position.
   a. Wait for the stage to stop moving.
xvi. Select VENT, remove the sample and SLOWLY close the door.
xvii. Put them machine back into stand-by state.
   a. Ensure High Vacuum is selected and select EVAC.

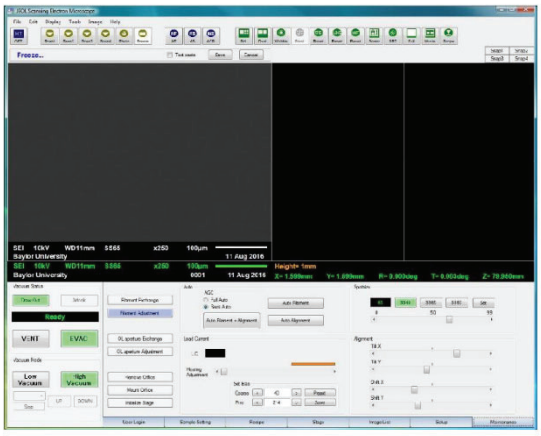

5

BIBLIOGRAPHY

1. Reed, A.S., D.C. Paine, and S. Lee, *Effect of O2 Fraction in the Sputter Gas on the Electrical Properties of Amorphous In-Zn-O and the Thin Film Transistor Performance.* Journal of Electronic Materials, 2016. **45**(12): p. 6310-6316.

2. Fortunato, E., et al., *High mobility amorphous/nanocrystalline indium zinc oxide deposited at room temperature.* Thin Solid Films, 2006. **502**(1-2): p. 104-107.

3. Fortunato, E., et al., *High mobility and low threshold voltage transparent thin film transistors based on amorphous indium zinc oxide semiconductors.* Solid-State Electronics, 2008. **52**(3): p. 443-448.

4. Choi, C.G., S.-J. Seo, and B.-S. Bae, *Solution-processed indium-zinc oxide transparent thin-film transistors.* Electrochemical and Solid-State Letters, 2008. **11**(1): p. H7-H9.

5. Lim, W., et al., *Room-Temperature-Deposited Indium-Zinc Oxide Thin Films with Controlled Conductivity.* Electrochemical and Solid-State Letters, 2007. **10**(9): p. H267-H269.

6. Wang, Y.-L., et al., *Room temperature deposited indium zinc oxide thin film transistors.* Applied physics letters, 2007. **90**(23): p. 232103.

7. Song, J.-I., et al., *Transparent amorphous indium zinc oxide thin-film transistors fabricated at room temperature.* Applied physics letters, 2007. **90**(2): p. 022106.

8. Nomura, K., et al., *Amorphous oxide semiconductors for high-performance flexible thin-film transistors.* Japanese journal of applied physics, 2006. **45**(5S): p. 4303.

9. Ito, N., et al., *Electrical and optical properties of amorphous indium zinc oxide films.* Thin Solid Films, 2006. **496**(1): p. 99-103.

10. Jung, Y.S., et al., *Influence of DC magnetron sputtering parameters on the properties of amorphous indium zinc oxide thin film.* Thin Solid Films, 2003. **445**(1): p. 63-71.

11. Barquinha, P., et al., *Influence of the semiconductor thickness on the electrical properties of transparent TFTs based on indium zinc oxide.* Journal of non-crystalline solids, 2006. **352**(9-20): p. 1749-1752.

12. Shinde, S., et al., *Optoelectronic properties of sprayed transparent and conducting indium doped zinc oxide thin films.* Journal of Physics D: Applied Physics, 2008. **41**(10): p. 105109.

13. Paine, D.C., et al., *Amorphous IZO-based transparent thin film transistors.* Thin Solid Films, 2008. **516**(17): p. 5894-5898.

14. Lee, S., H. Park, and D.C. Paine, *A study of the specific contact resistance and channel resistivity of amorphous IZO thin film transistors with IZO source–drain metallization.* Journal of Applied Physics, 2011. **109**(6): p. 063702.

15. Parthiban, S. and J.-Y. Kwon, *Role of dopants as a carrier suppressor and strong oxygen binder in amorphous indium-oxide-based field effect transistor.* Journal of Materials Research, 2014. **29**(15): p. 1585-1596.

16. Hosono, H., *Ionic amorphous oxide semiconductors: Material design, carrier transport, and device application.* Journal of Non-Crystalline Solids, 2006. **352**(9): p. 851-858.

17. Kamiya, T. and H. Hosono, *Material characteristics and applications of transparent amorphous oxide semiconductors.* Npg Asia Materials, 2010. **2**: p. 15.

18. Nomura, K., et al., *Room-temperature fabrication of transparent flexible thin-film transistors using amorphous oxide semiconductors.* Nature, 2004. **432**: p. 488.

19. Lee, S., et al., *Nanostructured Unsubstituted Polythiophene Films Deposited Using Oxidative Chemical Vapor Deposition: Hopping Conduction and Thermal Stability.* Advanced Materials Interfaces, 2018. **5**(9): p. 1701513.

20. Wiley Online Library. *Advanced Materials Interfaces*. Volume 5, Issue 9 2018 April 2, 2019].

21. Bellingham, J.R., W.A. Phillips, and C.J. Adkins, *Electrical and optical properties of amorphous indium oxide.* Journal of Physics: Condensed Matter, 1990. **2**(28): p. 6207-6221.

22. Minami, T., *Transparent conducting oxide semiconductors for transparent electrodes.* Semiconductor Science and Technology, 2005. **20**(4): p. S35-S44.

23. Lewis, B.G. and D.C. Paine, *Applications and Processing of Transparent Conducting Oxides.* MRS Bulletin, 2000. **25**(8): p. 22-27.

24. Hosono, H. *68.3: Invited Paper: Transparent Amorphous Oxide Semiconductors for High Performance TFT*. in *SID Symposium Digest of Technical Papers*. 2007. Wiley Online Library.

25. Barquinha, P., et al., *Effect of UV and visible light radiation on the electrical performances of transparent TFTs based on amorphous indium zinc oxide.* Journal of non-crystalline solids, 2006. **352**(9-20): p. 1756-1760.

26. Kim, M.S., et al., *Growth and characterization of indium-doped zinc oxide thin films prepared by sol-gel method.* Acta Physica Polonica-Series A General Physics, 2012. **121**(1): p. 217.

27. Lee, S., B. Bierig, and D.C. Paine, *Amorphous structure and electrical performance of low-temperature annealed amorphous indium zinc oxide transparent thin film transistors.* Thin Solid Films, 2012. **520**(10): p. 3764-3768.

28. Lee, S. and D.C. Paine, *Identification of the native defect doping mechanism in amorphous indium zinc oxide thin films studied using ultra high pressure oxidation.* Applied Physics Letters, 2013. **102**(5): p. 052101.

29. Leenheer, A.J., et al., *General mobility and carrier concentration relationship in transparent amorphous indium zinc oxide films.* Physical Review B, 2008. **77**(11): p. 115215.

30. Sun, J., Y. Huang, and H. Gong, *Improved mobility and conductivity of an Al2O3 incorporated indium zinc oxide system.* Journal of Applied Physics, 2011. **110**(2): p. 023709.

31. Lee, S., K. Park, and D.C. Paine, *Metallization strategies for In2O3-based amorphous oxide semiconductor materials.* Journal of Materials Research, 2012. **27**(17): p. 2299-2308.

32. Medvedeva, J.E., D.B. Buchholz, and R.P.H. Chang, *Recent Advances in Understanding the Structure and Properties of Amorphous Oxide Semiconductors.* Advanced Electronic Materials, 2017. **3**(9): p. 1700082.

33. Gleskova, H. and S. Wagner, *Electron mobility in amorphous silicon thin-film transistors under compressive strain.* Applied Physics Letters, 2001. **79**(20): p. 3347-3349.

34. Chong, E., Y.S. Chun, and S.Y. Lee, *Amorphous silicon–indium–zinc oxide semiconductor thin film transistors processed below 150 C.* Applied Physics Letters, 2010. **97**(10): p. 102102.

35. Paine, D.C., et al., *A study of low temperature crystallization of amorphous thin film indium–tin–oxide.* Journal of Applied Physics, 1999. **85**(12): p. 8445-8450.

36. Lee, G.J., et al., *High performance, transparent a-IGZO TFTs on a flexible thin glass substrate.* Semiconductor Science and Technology, 2014. **29**(3): p. 035003.

37. Chong, E., Y.S. Chun, and S.Y. Lee, *Amorphous silicon–indium–zinc oxide semiconductor thin film transistors processed below 150 °C.* Applied Physics Letters, 2010. **97**(10): p. 102102.

38. Yaglioglu, B., H.-Y. Yeom, and D.C. Paine, *Crystallization of amorphous In2O3–10 wt % ZnO thin films annealed in air.* Applied Physics Letters, 2005. **86**(26): p. 261908.

39. Jeong, S., et al., *Role of gallium doping in dramatically lowering amorphous-oxide processing temperatures for solution-derived indium zinc oxide thin-film transistors.* Advanced Materials, 2010. **22**(12): p. 1346-1350.

40. Kang, D., et al., *Amorphous gallium indium zinc oxide thin film transistors: Sensitive to oxygen molecules.* Applied physics letters, 2007. **90**(19): p. 192101.

41. Jeon, J.-W., et al., *Effect of annealing temperature on optical band-gap of amorphous indium zinc oxide film.* Journal of Alloys and Compounds, 2011. **509**(41): p. 10062-10065.

42. Chong, E., S.H. Kim, and S.Y. Lee, *Role of silicon in silicon-indium-zinc-oxide thin-film transistor.* Applied Physics Letters, 2010. **97**(25): p. 252112.

43. Chong, E., et al., *The relationship between processing parameters and the performance of novel amorphous silicon–indium–zinc oxide thin film transistors.* Current Applied Physics, 2011. **11**(4, Supplement): p. S132-S134.

44. Kim, C.-J., et al., *Amorphous hafnium-indium-zinc oxide semiconductor thin film transistors.* Applied Physics Letters, 2009. **95**(25): p. 252103.

45. Chang, S.-P. and S.-S. Shih, *Amorphous hafnium-indium-zinc oxide semiconductor thin film transistors.* Journal of Nanomaterials, 2012. **2012**: p. 113.

46. Chong, E., K.C. Jo, and S.Y. Lee, *High stability of amorphous hafnium-indium-zinc-oxide thin film transistor.* Applied Physics Letters, 2010. **96**(15): p. 152102.

47. Kim, S., et al., *Carrier transport mechanism of Mo contact to amorphous hafnium indium zinc oxides.* physica status solidi (a), 2014. **211**(8): p. 1818-1821.

48. Li, Y.L., et al., *Effect of oxygen concentration on properties of indium zinc oxide thin films for flexible dye-sensitized solar cell.* Japanese Journal of Applied Physics, 2008. **47**(8S2): p. 6896.

49. Park, S.C., et al., *Advanced photo-annealing of indium zinc oxide films for thin-film transistors using pulse UV light.* Journal of Information Display, 2016. **17**(1): p. 1-7.

50. Socratous, J., et al., *Energy-dependent relaxation time in quaternary amorphous oxide semiconductors probed by gated Hall effect measurements.* Physical Review B, 2017. **95**(4): p. 045208.

51. Liu, J., et al., *High-Performance Flexible Transparent Thin-Film Transistors Using a Hybrid Gate Dielectric and an Amorphous Zinc Indium Tin Oxide Channel.* Advanced Materials, 2010. **22**(21): p. 2333-2337.

52. Munzenrieder, N., K.H. Cherenack, and G. Troster, *The effects of mechanical bending and illumination on the performance of flexible IGZO TFTs.* IEEE Transactions on Electron Devices, 2011. **58**(7): p. 2041-2048.

53. Schwab, K. *The Fourth Industrial Revolution: What It Means and How to Respond*. 2015 April 3rd, 2019]; Available from: https://www.foreignaffairs.com/articles/2015-12-12/fourth-industrial-revolution.

54. Davis, N. *What is the fourth industrial revolution?* Global Agenda 2016 April 3, 2019]; Available from: https://www.weforum.org/agenda/2016/01/what-is-the-fourth-industrial-revolution/.

55. Ohering, M., *Materials Science of Thin Films Deposition and Structure*. 2002, Academic Press, San Diego.

56. Wasa, K., M. Kitabatake, and H. Adachi, *Thin film materials technology: sputtering of control compound materials*. 2004: Springer Science & Business Media.

57. Klauk, H., *Organic thin-film transistors.* Chemical Society Reviews, 2010. **39**(7): p. 2643-2666.

58. Kumar, N., *Comprehensive physics XII*. 2004: Laxmi Publications.

59. Morikawa, H. and M. Fujita, *Crystallization and electrical property change on the annealing of amorphous indium-oxide and indium-tin-oxide thin films.* Thin Solid Films, 2000. **359**(1): p. 61-67.

60. Demaurex, B., et al., *Damage at hydrogenated amorphous/crystalline silicon interfaces by indium tin oxide overlayer sputtering.* Applied Physics Letters, 2012. **101**(17): p. 171604.

61. Fortunato, E.M., et al., *High mobility indium free amorphous oxide thin film transistors.* Applied Physics Letters, 2008. **92**(22): p. 222103.

62. Cho, D.H., et al. *21.2: Al and Sn-Doped Zinc Indium Oxide Thin Film Transistors for AMOLED Back-Plane*. in *SID Symposium Digest of Technical Papers*. 2009. Wiley Online Library.

63. Fortunato, E., et al., *Transparent conducting oxides for photovoltaics.* MRS bulletin, 2007. **32**(3): p. 242-247.

64. Sasabayashi, T., et al., *Comparative study on structure and internal stress in tin-doped indium oxide and indium-zinc oxide films deposited by rf magnetron sputtering.* Thin Solid Films, 2003. **445**(2): p. 219-223.

65. Ow-Yang, C.W., et al., *A time-resolved reflectivity study of the amorphous-to-crystalline transformation kinetics in dc-magnetron sputtered indium tin oxide.* Journal of applied physics, 1998. **83**(1): p. 145-154.

66. Walker, D.E., et al., *High mobility indium zinc oxide thin film field-effect transistors by semiconductor layer engineering.* ACS applied materials & interfaces, 2012. **4**(12): p. 6835-6841.

67. De Wit, J., G. Van Unen, and M. Lahey, *Electron concentration and mobility in In2O3.* Journal of Physics and Chemistry of Solids, 1977. **38**(8): p. 819-824.

68. Jeong, J.K., *Photo-bias instability of metal oxide thin film transistors for advanced active matrix displays.* Journal of Materials Research, 2013. **28**(16): p. 2071-2084.

69. Shin, Y., et al., *The mobility enhancement of indium gallium zinc oxide transistors via low-temperature crystallization using a tantalum catalytic layer.* Scientific reports, 2017. **7**(1): p. 10885.

70. Lan, L., et al., *Enhancement of bias and illumination stability in thin-film transistors by doping InZnO with wide-band-gap Ta2O5.* Applied Physics Letters, 2013. **102**(24): p. 242102.

71. Campet, G., et al., *The electronic effect of Ti4+, Zr4+ and Ge4+ dopings upon the physical properties of In2O3 and Sn-doped In2O3 ceramics: application to new highly-transparent conductive electrodes.* Materials Science and Engineering: B, 1993. **19**(3): p. 285-289.

72. Sun, J. and H. Gong, *Abrupt resistivity decrease and other unexpected phenomena in a doped amorphous ternary metal oxide.* Applied Physics Letters, 2010. **97**(9): p. 092106.

73. Kerr, J.A., *CRC handbook of chemistry and physics.* CRC Press: Boca Raton, FL, 2000. **2001**: p. 9-51.

74. Gösele, U. and K.N. Tu, *Growth kinetics of planar binary diffusion couples: ''Thin-film case'' versus ''bulk cases''.* Journal of Applied Physics, 1982. **53**(4): p. 3252-3260.

75. Hardy, N. *Thin Film Deposition By Sputtering: Essential Basics*. News & Articles [Online] 2013 October 7, 2013 17-Oct-2018]; Available from: http://www.semicore.com/news/70-thin-film-deposition-sputtering.

76. Hughes, M. *What is DC Sputtering?* News & Articles [Online] 2016 November 26, 2016 17-Oct-2018]; Available from: http://www.semicore.com/news/94-what-is-dc-sputtering.

77. Hughes, M. *What is RF Sputtering?* News & Articles [Online] 2016 October 27, 2016 17-Oct-2018]; Available from: http://www.semicore.com/news/92-what-is-rf-sputtering.

78. Lee, S. and D.C. Paine, *On the effect of Ti on the stability of amorphous indium zinc oxide used in thin film transistor applications.* Applied Physics Letters, 2011. **98**(26): p. 262108.

79. National Institute of Standards & Technology. *Resistivity and Hall Measurements*. 2010 April 2, 2019]; Available from: https://www.nist.gov/pml/engineering-physics-division/popular-links/hall-effect/resistivity-and-hall-measurements.

80. Smits, F.M., *Measurement of sheet resistivities with the four-point probe.* The Bell System Technical Journal, 1958. **37**(3): p. 711-718.

81. National Institute of Standards & Technology. *The Hall Effect*. 2010 April 2, 2019]; Available from: https://www.nist.gov/pml/engineering-physics-division/popular-links/hall-effect/hall-effect.

82. Nave, C.R. *Bragg's Law*. 2016 [cited April 2, 2019; Available from: http://hyperphysics.phy-astr.gsu.edu/hbase/quantum/bragg.html.

83. Darrell Henry, N.E., John Goodge, David Mogk. *X-ray reflection in accordance with Bragg's Law*. Geochemical Instrumentation and Analysis 2016 [cited April 2, 2019; Available from: https://serc.carleton.edu/research_education/geochemsheets/BraggsLaw.html.

84. Royal Society of Chemistry, *Spectroscopy in a Suitcase students' resource: Ultraviolet - Visible Spectroscopy (UV)*, in *LearnChemistry: Enhancing learning and teaching*. 2009.

85. Faculty of Health and Wellbeing: Biosciences Division. *Resources for Analytical Science: Beer's Law*. n.d. April 2, 2019]; Available from: https://teaching.shu.ac.uk/hwb/chemistry/tutorials/molspec/beers1.htm.

86. what-when-how In Depth Tutorials and Information. *Energy Bands in Crystals (Fundamentals of Electron Theory) Part 3*. 03/22/2019]; Available from: http://what-when-how.com/electronic-properties-of-materials/energy-bands-in-crystals-fundamentals-of-electron-theory-part-3/.

87. Pradhan, D. and K.T. Leung, *Controlled growth of two-dimensional and one-dimensional ZnO nanostructures on indium tin oxide coated glass by direct electrodeposition.* Langmuir, 2008. **24**(17): p. 9707-9716.

88. Burstein, E., *Anomalous Optical Absorption Limit in InSb.* Physical Review, 1954. **93**(3): p. 632-633.

89. Shan, F.K. and Y.S. Yu, *Band gap energy of pure and Al-doped ZnO thin films.* Journal of the European Ceramic Society, 2004. **24**(6): p. 1869-1872.

90. Sernelius, B.E., et al., *Band-gap tailoring of ZnO by means of heavy Al doping.* Physical Review B, 1988. **37**(17): p. 10244-10248.

91. Mass, J., P. Bhattacharya, and R.S. Katiyar, *Effect of high substrate temperature on Al-doped ZnO thin films grown by pulsed laser deposition.* Materials Science and Engineering: B, 2003. **103**(1): p. 9-15.

92. Wang, A., et al., *Charge transport, optical transparency, microstructure, and processing relationships in transparent conductive indium–zinc oxide films grown by low-pressure metal-organic chemical vapor deposition.* Applied Physics Letters, 1998. **73**(3): p. 327-329.

93. Cremer, R., et al., *Sputter deposition of crystalline alumina coatings.* Surface and Coatings Technology, 2003. **163-164**: p. 157-163.

94. Segda, B.G., M. Jacquet, and J.P. Besse, *Elaboration, characterization and dielectric properties study of amorphous alumina thin films deposited by r.f. magnetron sputtering.* Vacuum, 2001. **62**(1): p. 27-38.

95. Oh, M.S., et al., *Improving the Gate Stability of ZnO Thin-Film Transistors with Aluminum Oxide Dielectric Layers.* Journal of The Electrochemical Society, 2008. **155**(12): p. H1009-H1014.

96. Argall, F. and A.K. Jonscher, *Dielectric properties of thin films of aluminium oxide and silicon oxide.* Thin Solid Films, 1968. **2**(3): p. 185-210.

97. Fisher, J.C. and I. Giaever, *Tunneling Through Thin Insulating Layers.* Journal of Applied Physics, 1961. **32**(2): p. 172-177.

98. Rose, V. and R. Franchy, *The band gap of ultrathin amorphous and well-ordered Al2O3 films on CoAl(100) measured by scanning tunneling spectroscopy.* Journal of Applied Physics, 2009. **105**(7): p. 07C902.

99. Costina, I. and R. Franchy, *Band gap of amorphous and well-ordered Al2O3 on Ni3Al(100).* Applied Physics Letters, 2001. **78**(26): p. 4139-4141.